



Chair of Reservoir Engineering

Master's Thesis



Emulsion Characterization During
Displacement in Simple Pore Geometries

Judy Jalkh

September 2022



AFFIDAVIT

I declare on oath that I wrote this thesis independently, did not use other than the specified sources and aids, and did not otherwise use any unauthorized aids.

I declare that I have read, understood, and complied with the guidelines of the senate of the Montanuniversität Leoben for "Good Scientific Practice".

Furthermore, I declare that the electronic and printed version of the submitted thesis are identical, both, formally and with regard to content.

Date 15.09.2022

A handwritten signature in black ink, appearing to read 'Judy Jalkh', positioned above a horizontal line.

Signature Author
Judy Jalkh

Judy Jalkh

Master Thesis 2022

Petroleum Engineering

Emulsion Characterization During Displacement in Simple Pore Geometries

Supervisor: Univ.-Prof. Dipl.-Phys. Dr.rer.nat.
Holger Ott.

Co-supervisor/Advisor: Dipl.-Ing. Ahmad
Kharrat.

Chair of Reservoir Engineering

To all my loved ones.

Acknowledgements

I would like to express my sincere gratitude to my supervisor Dipl. Ing Ahmad Kharrat for his invaluable guidance and encouragement that helped me throughout my research.

This work would not have been possible without the constant support of my love, thank you very much.

Abstract

Waterflooding and Enhanced Oil Recovery (EOR) techniques are known to be viable options in oil recovery. Operators worldwide implement these techniques to maintain reservoir pressure, increase oil recovery, and prolong the overall life cycle of the production area. While each method theoretically behaves according to a specific physical phenomenon, how it manifests in real life differs from one field to another. Thus, experimenting with these techniques through lab work and simulations before their application in the field is crucial to achieving the desired outcome and optimizing the injection process by how, when, where, and what to inject. One method for studying such fluid movement is in the microfluidic genre, implementing a Lab on a chip (LOC) approach because it allows the measurement and the visualization of the physical phenomena at a detailed level on the pore scale. LOC allows altering flow configurations and parameters to understand their effects on fluid displacement and flow regimes fully.

For this reason, this thesis is based on the LOC method. Several chip designs with varying properties, such as aspect ratio and distance between pores, were used. Fluids with different chemical compositions, such as surfactant, alkaline solutions, and distilled water, were injected at different rates. Doing so allowed us to see how the injected fluid's compositions affect the flow and how the available pore design aids or hinders successful recovery. In other words, we analyzed the situation from two points of view: the manipulation of (a) the injected fluid and (b) the shape of the flow passages. Thus, we can develop a general theory of what to expect when details about the pore structure are known. Our experiments were analyzed at three-time intervals: first contact displacement (i.e., when the injected mixture first meets the displaced phase), during continuous displacement, and at the final stages. The analysis included front shape, remaining oil saturation, emulsion formation, and velocity calculation. Our results for low-rate fluid injection into a decane-filled pore system prove that aspect ratio affects our studied parameters. We are revealing that with an increasing aspect ratio (for the constant distance between pores), the front velocity and stability and the amount of remaining oil increase. Altering the salinity of the injected surfactant similarly affects these parameters and the degree of solubilization of decane in water.

Zusammenfassung

Wasserflutungen und Enhanced Oil Recovery (EOR)-Techniken sind als praktikable Optionen für die Ölförderung bekannt. Operatoren auf der ganzen Welt setzen diese Techniken ein, um den Druck in der Lagerstätte aufrechtzuerhalten, die Ölförderung zu erhöhen und den Lebenszyklus des Fördergebiets zu verlängern. Während sich jede Methode theoretisch entsprechend eines bestimmten physikalischen Phänomens verhält, ist es in der Praxis von Feld zu Feld unterschiedlich, welchen Effekt es erzielt. Daher ist das Experimentieren mit diesen Techniken im Labor und in Simulationen vor ihrer Anwendung im Feld entscheidend für das Erreichen des gewünschten Ergebnisses, und die Optimierung der Injektionen, wie, wann, wo und was eingespritzt werden soll. Eine Methode zur Untersuchung solcher Flüssigkeitsbewegungen ist die Mikrofluidik, die einen Lab on a chip (LOC)-Ansatz verfolgt, da sie die Messung und Visualisierung der physikalischen Phänomene auf eine detaillierte Art auf Porenebene ermöglicht. LOC ermöglicht die Veränderung von Strömungskonfigurationen und -parametern, um deren Auswirkungen auf die Flüssigkeitsverschiebung und die Strömungsregime vollständig zu verstehen.

Aus diesem Grund basiert diese Arbeit auf der LOC-Methode. Es wurden mehrere Chipdesigns mit unterschiedlichen Eigenschaften, wie z. B. Seitenverhältnis und Abstand zwischen den Poren, verwendet. Flüssigkeiten mit unterschiedlichen chemischen Zusammensetzungen, wie Tenside, basische Lösungen und destilliertes Wasser, wurden mit verschiedenen Geschwindigkeiten eingespritzt. Auf diese Weise konnten wir feststellen, wie sich die Zusammensetzung der eingespritzten Flüssigkeit auf die Strömung auswirkt und wie das vorhandene Porendesign eine erfolgreiche Förderung unterstützt oder behindert. Mit anderen Worten, wir analysierten die Situation aus zwei Blickwinkeln: die Manipulation (a) der eingespritzten Flüssigkeit und (b) der Form der Fließkanäle. So können wir eine allgemeine Theorie darüber entwickeln, was zu erwarten ist, wenn Details über die Porenstruktur bekannt sind. Unsere Experimente wurden in drei Zeitintervallen analysiert: bei der ersten Kontaktverschiebung (d. h. wenn das eingespritzte Gemisch zum ersten Mal auf die verdrängte Phase trifft), während der kontinuierlichen Verdrängung und in den Endphasen. Die Analyse umfasste die Form der Front, die verbleibende Ölsättigung, die Emulsionsbildung und die Geschwindigkeitsberechnung. Unsere Ergebnisse für die Flüssigkeitseinspritzung mit niedriger Geschwindigkeit in einem mit Dekan gefüllten Porensystem zeigen, dass das Seitenverhältnis

die untersuchten Parameter beeinflusst. Es zeigt sich, dass mit zunehmendem Aspekt-Verhältnis (bei konstantem Abstand zwischen den Poren) die Frontgeschwindigkeit und -stabilität sowie die Menge des verbleibenden Öls zunehmen. Die Veränderung des Salzgehalts des eingespritzten Tensids wirkt sich vergleichbar auf diese Parameter und die Löslichkeit von Dekan in Wasser aus.

Table of Contents

Acknowledgements.....	v
Abstract.....	vii
Zusammenfassung.....	viii
Chapter 1.....	13
Introduction.....	13
1.1 Problem Description	13
1.2 Scope and Objectives.....	13
Chapter 2.....	15
Literature Review.....	15
2.1 Oil Recovery and EOR	15
2.2 Surfactants and Alkaline.....	19
2.3 Emulsions.....	24
2.4 Micromodels	26
Chapter 3.....	32
Experimental Equipment	32
3.1 Porous Medium.....	32
3.2 Instrumentation	33
3.3 Fluids	34
Chapter 4.....	37
Experimental Procedure.....	37
4.1 Cleaning Procedure.....	37
4.2 Experimental Procedure.....	37
4.3 Calculations.....	38
Chapter 5.....	41
Results & Discussion	41
5.1 Reynold's Number:	41
5.2 Generic fluids — Different ARs, $\lambda=100\ \mu\text{m}$, Low Injection rate (0.0008 ml/h)	42
5.3 Generic fluids — Different λ , AR =8, Low Injection rate (0.0008 ml/h)	64
5.4 Generic fluids — Different Injection rates, ARs =1.6 & 3.2, same λ	67
5.5 Crude Oil — different AR, $\lambda=100\ \mu\text{m}$, and low injection rate (0.0008 ml/h)	71
5.6 Summary	76
Chapter 6.....	77
Conclusion	77
6.1 Summary	77
6.2 Evaluation	78
6.3 Future work.....	78

References.....	79
List of Figures.....	83
List of Tables.....	85
Nomenclature.....	86
Abbreviations.....	87

Chapter 1

Introduction

1.1 Problem Description

Increasing production from existing reservoirs and maintaining longer production plateaus require the implementation of secondary recovery (waterflooding), and/or tertiary recovery (EOR). To properly study the effects of these technologies and predict their success in the field, it is important to study fluid-fluid interactions and displacement mechanisms. While studying two phase flow, two factors must be taken into consideration. The first is the different chemical compositions of the fluids and the second is the characteristics and properties of the pore structure. In the past decade, microfluidics and Lab on a Chip (LOC) have been center stage because of its flexibility for assembling different flow configurations and observing transport phenomena at the microscale. LOC allows the visualization of fluid interfaces and emulsion formation on a more detail level. This is beneficial because emulsions, which involve the dispersion of one phase in the other as droplets, are very important in the displacement process, final recovery factor, and amount of oil trapped in place.

1.2 Scope and Objectives

This thesis uses the LOC approach to investigate the effects of pore geometry and surfactant salinity on the displacement process in terms of front shape, front velocity, amount of remaining oil, and emulsion formation. All will be studied at first contact displacement (i.e. when the injected mixture first contacts the displaced phase), while the emulsions will also be studied at a later stage to see how they change with time. We will be studying emulsification and fluid displacement by not only altering the fluids in place and injected in terms of salinity, type of oil in place, and injected fluid rate, but by also changing the pore network characteristics in terms of aspect ratio, pore bodies and throats sizes, and distance between the pores. The end

goal is coming up with a general theory that allows us to predict how the emulsification and displacement processes will look when the subsurface structure has those specific properties.

Chapter 2

Literature Review

2.1 Oil Recovery and EOR

While technologies that produce energy from renewable resources like solar, wind, or water are gaining momentum and becoming more advanced and affordable, fossil fuel consumption, namely oil and gas, will still be needed to satisfy the ever-increasing worldwide energy demand fueled by exponential population growth, motivated industrial development, and speedy world economy and prosperity evolution. In fact, in 2040 this energy increase is estimated to be 30% compared to 2010 (Karatayev et al., 2018 [15]), with oil consumption of around 111.1 million barrels/day (Zhang et al., 2020 [34]). According to the sustainability report published by Royal Dutch Shell in 2013 [25], absolute fossil fuel demand will peak in 2040 and gradually decline. But even with this decline, by 2050, 70% of the energy demand will still be supplied by fossil fuels.

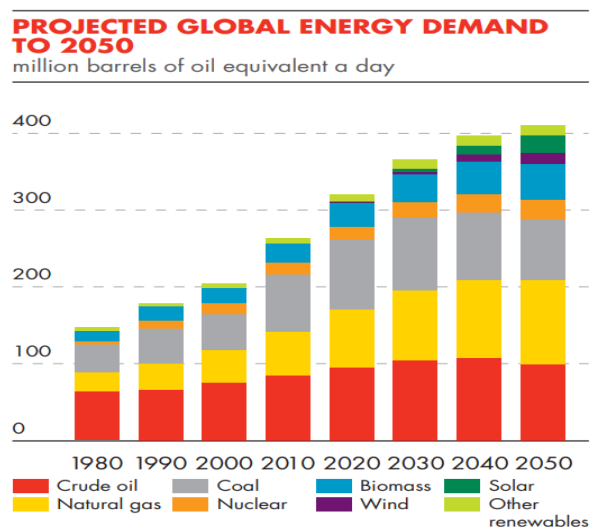


Figure 1. Projected global energy demand to 2050. (Royal Dutch Shell, 2013 [25])

Oil recovery goes through three phases:

1. Primary phase

It is the conventional oil recovery. On average, 30% of the original oil in place (OOIP) is produced in this phase with the help of natural flow drives and artificial lift (Pogaku et al., 2017 [23]; Saravanan and Keerthana, 2017 [26]). Natural flow drives indicate that production occurs due to the fluid's in situ pressure without tampering. These drives can either work alone or in combination with each other (Gyan et al., 2019 [10]). These natural drives are solution-gas drive, gas-cap drive, water drive, rock and liquid expansion, and gravity drainage.

Over some (limited) time, the pressure gradient begins to drop due to the continuous oil or gas production leading to the inevitable decrease in production rate governed by Darcy's Law. Artificial lift steps in to increase production rates in the primary phase. Its main goal is to decrease the bottom hole pressure by increasing the drawdown pressure of the producing well.

2. Secondary phase:

The decision to move on to the secondary phase is reached when the primary phase reaches a limiting economic threshold, and new techniques are needed to keep the reservoir alive. Here is where tampering with the in-situ reservoir environment begins. Secondary recovery aims to maintain reservoir pressure by injecting water or gas.

Waterflooding has been one of the most economical and successful methods for oil recovery because water is an efficient displacing agent for light to medium oils. Additionally, it is easier to handle and inject than other substances, thus decreasing the operating costs, and it is widely available making it inexpensive (Yousef et al., 2011 [33]). In recent years, a large amount of research and trials has been dedicated to an updated version of traditional waterflooding called smart or engineered waterflooding (Yousef et al., 2011 [33]). It allows the modification of the injected water's many characteristics in order to perfectly satisfy each reservoir's demand for letting go of its oil.

However, due to reservoir heterogeneities and in-situ oil-water surface tension, additional oil recovery is constrained, and the oil is either trapped or bypassed.

3. Tertiary phase- usually referred to as enhanced oil recovery (EOR):

Tertiary recovery is done to additionally increase oil recovery by injecting different types of fluids. EOR techniques are continuously being researched and studied to further understand the mechanisms that govern this additional recovery, optimize them depending on the given reservoir, and invent new techniques. EOR improves one or both of the following efficiencies:

volumetric sweep efficiency and displacement efficiency. Sweep efficiency is governed by reservoir heterogeneity and mobility. Thus, mobility can be improved by altering the mobility of the injected fluid or the in-situ fluid. Displacement efficiency is governed by capillarity. Capillary forces cause the matrix to hold on tight to the oil and prevent it from being produced. By injecting different types of chemicals or gases, capillarity can be affected. Finally, the ultimate displacement efficiency E will be improved according to the 2.1 and 2.2 equations (Green and Willhite, 2008 [9]):

Where:

- E = Ultimate efficiency
- E_D = Microscopic displacement efficiency
- E_V = Macroscopic/volumetric displacement efficiency
- S_{oi} = Initial oil in place
- S_{or} = Residual oil

$$E = E_D \times E_V \tag{2.1}$$

$$E_D = \frac{S_{oi} - S_{or}}{S_{oi}} \tag{2.2}$$

Ultimately, EOR improves oil recovery by affecting one or a combination of the following properties: viscosity (injected or produced fluid), rock wettability, interfacial tension (IFT), capillary forces, and mobility ratio.

- Mobility ratio:

Mobility describes the immiscible fluid's capability of displacing the oil (Donaldson and Alam, 2008 [6]). It behaves according to equation 2.3:

$$M = \frac{\lambda_D}{\lambda_d} = \frac{\frac{k_{r,D}}{\mu_D}}{\frac{k_{r,d}}{\mu_d}} = \frac{k_{r,D} \times \mu_d}{k_{r,d} \times \mu_D} \tag{2.3}$$

Where:

- M = Mobility ratio

- λ = Phase mobility
- μ = Viscosity
- k_r = Relative permeability
- Index d = Displaced phase
- Index D = Displacing phase

A mobility ratio of less than 1 is optimum to avoid viscous or capillary fingering (Sheng, 2011 [28]). By looking at equation 2.3, it is clear that by manipulating the viscosities of the phase (increasing the viscosity of displacing phase and decreasing the viscosity of the displaced phase) or by reducing the relative permeability of the displaced fluid, fingering can be avoided.

Not all EOR methods can exclusively affect the mobility ratio. For example, combining surfactant and polymer flooding instead of only surfactant flooding will increase the water viscosity (displacing viscosity) and reduce the IFT simultaneously (Sun et al., 2020 [29]).

- Capillary Number:

Capillary number allows us to identify whether the fluid in place is trapped or mobile by comparing the viscous forces (F_v) and the capillary forces (F_c), which trap the fluid. It behaves according to equation 2.4 (Sheng, 2011 [28]).

$$N_c = \frac{F_v}{F_c} = \frac{v \times \mu}{\sigma}$$

2.4

Where:

- N_c = Capillary number
- F_v = Viscous forces
- F_c = Capillary forces
- v = Pore flow velocity of the displacing fluid
- μ = Viscosity of the displacing fluid
- σ = IFT between the displacing and the displaced phase

As seen in Figure 2, EOR methods fall under four categories: Gas injection, thermal, chemical, and other.

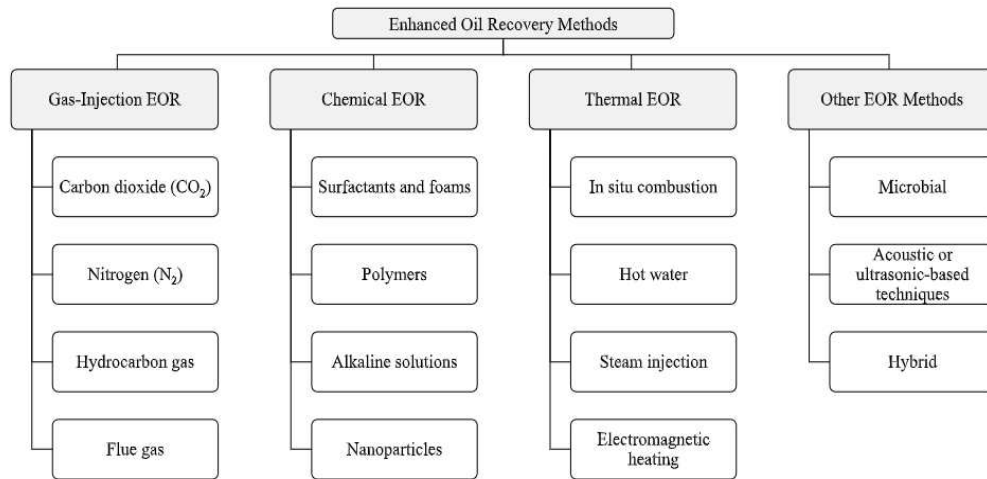


Figure 2. Main methods of EOR (Massarweh & Abushaikha, 2020 [22])

This thesis deals with chemical EOR, mainly surfactant injection and alkaline injection. Surfactants are popular in the oil and gas industry due to their ability to alter not only the properties of the rock matrix surface but also the oil-water interface as well (Zulkifli et al., 2019 [37]). As for alkaline flooding, it is almost the same as the prior, but instead of making the surfactants at the surface and then injecting them, alkaline injection generates the surfactant in-situ from the reaction of the natural organic acids in the oil with the injected alkalis. Both of these methods increase oil recovery by reducing IFT, altering the wettability, and generating foam or emulsions (Johnson, 1976 [14]). Johnson also mentioned that the injected and in-situ fluid properties and the rock formation affect how each mechanism will play out (Johnson, 1976 [14]).

2.2 Surfactants and Alkaline

2.2.1 Definition

All surfactants are made of a hydrophilic head and a hydrophobic/lipophilic tail i.e., the head dissolves in the aqueous phase, and the tail dissolves in the oleic phase. The charge of their hydrophilic head determines their classification, which is shown in Table 1 (Kume et al., 2007 [17]):

Table 1. Surfactant Classification is based on head charge.

Hydrophilic head charge	Classification	Usage
No charge	Non-ionic	<ul style="list-style-type: none"> • Usually used as co-surfactants with Anionic • Improve system phase behavior. • Have high tolerance to salinity. (Sheng, 2011)
Negative charge	Anionic	<ul style="list-style-type: none"> • Most popular in the petroleum industry. (Azam et al., 2013)
Positive charge	Cationic	<ul style="list-style-type: none"> • Not used with sandstones. • Used with carbonates with small silicone occurrences. • Help with wettability alteration in carbonates. (Ma et al., 2013)
Both negative and positive charge	Zwitterionic/Amphoteric	<ul style="list-style-type: none"> • Most expensive • Better performance in high temperature and high salinity environments (Sheng, 2011)

As for alkaline flooding, it behaves similarly to surfactant flooding but instead forms a surfactant in the reservoir (in-situ) when the injected alkaline agent reacts with the acidic components found in the reservoir oil. Thus, different surfactants are made depending on the type of acids in the reservoir.

2.2.2 Characterization

2.2.2.1 Critical micelle concentration

According to (Massarweh & Abushaikha, 2020 [22]), a micelle is "an aggregate from surfactant molecules dispersed in a liquid colloid." Surfactants need to reach a minimum concentration to aggregate. This is referred to as the critical micelle concentration (CMC). The CMC varies from one surfactant to another because it depends on pressure, temperature, pH, ionic composition, salinity, and surfactant molecular structure (Harutyunyan and Harutyunyan, 2019 [13]). The CMC can be measured using direct and indirect methods. Some examples are dye adsorption, surface tension, solubilization (Suzuki, 1970 [30]), and IFT measurement, which is mainly used for EOR applications (Haq et al., 2020 [12]).

As seen in Figure 3, when surfactants first enter the system, they tend to accumulate at the oil-water interface. As more surfactants are introduced and their concentration increases, the IFT decreases sharply until it reaches its minimum point at the CMC. At the CMC, micelles start forming. Any increase in concentration beyond that point no longer affects the IFT but instead increases the number of micelles present in the aqueous solution (Sheng, 2011 [28]).

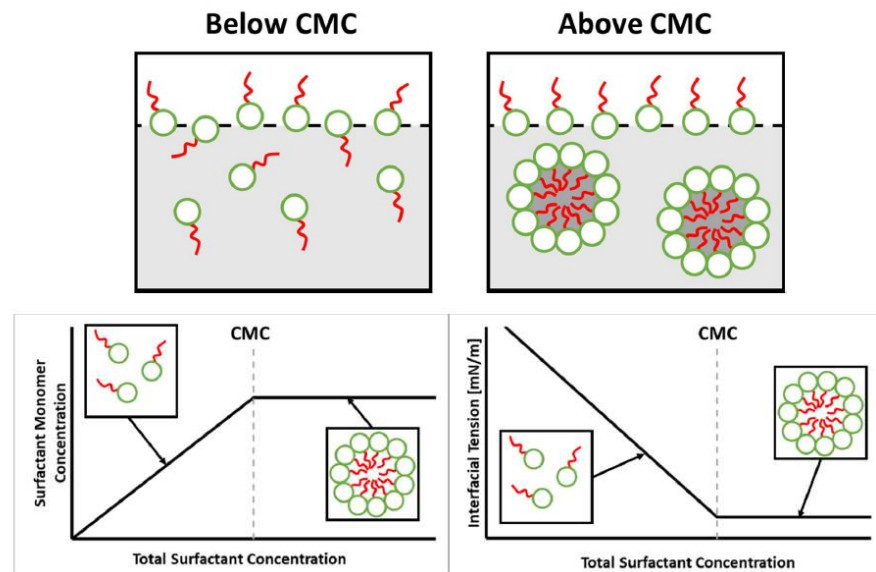


Figure 3. Surfactant concentration below and above CMC, with respect to surfactant monomer concentration and IFT. (Lake, 2014 [18])

2.2.2.2 Solubilization parameters

The solubilization parameters play an important role in optimizing oil recovery because usually, the lowest oil water IFT is achieved at the optimum salinity. The solubilization ratio of a single

phase is defined as the volume of that phase solubilized per volume of surfactant in a microemulsion phase. Its equation is as follows (Abalkhail et al., 2020 [1]) (2.5, 2.6):

$$SR_{oil} = \frac{Volume_{oil}}{Volume_{surfactant}} \quad 2.5$$

$$SR_{water} = \frac{Volume_{water}}{Volume_{surfactant}} \quad 2.6$$

When $SR_{oil} = SR_{water}$, optimum solubilization is reached, and ideal microemulsion formulation occurs (Hamidi et al., 2015 [11]).

2.2.2.3 Microemulsion Winsor systems and Winsor Ratio

Winsor, 1948 [31] developed two methods for microemulsion and phase behavior understanding, one being qualitative and the other quantitative. The microemulsion systems are four classifications of emulsions based on their description. These are referred to as Winsor Type and can be seen in Figure 4.

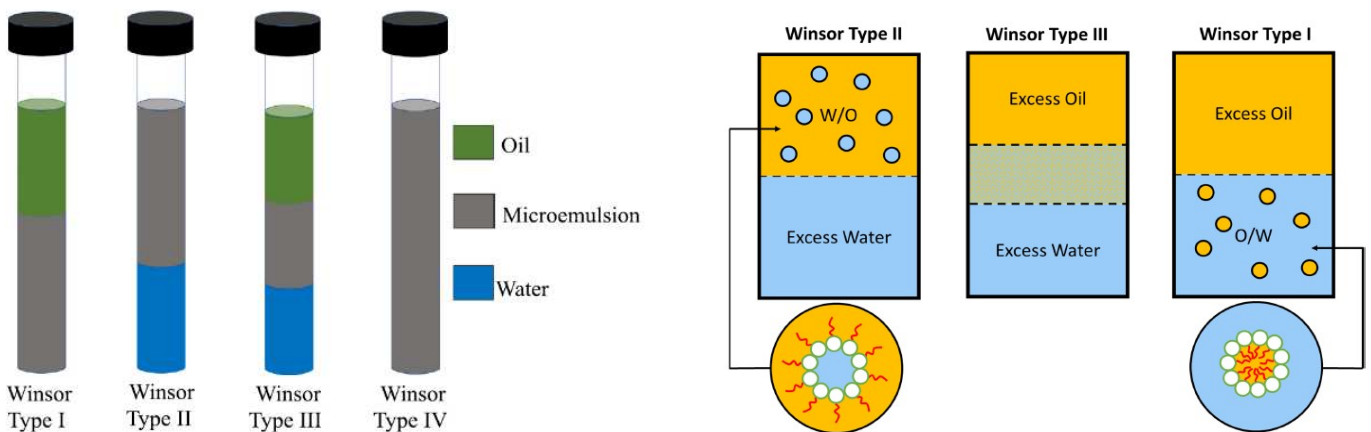


Figure 4. Winsor classification of microemulsions. (Winsor, 1948 [31])

Winsor ratio, on the other hand, is a quantitative method where R is calculated according to equation 2.7:

$$WR = \frac{E_{Tail-Oil}}{E_{Head-Brine}}$$

2.7

Where:

E tail-oil: attractive force between the surfactant tail (lipophilic) and the oil phase

E head-brine: attractive force between surfactant head (hydrophilic) and the water phase

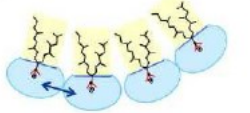
It is important to note that these interactions and attractive forces are sensitive to temperature, tail length, oil type and composition, head type, co-solvent, and salinity. For example, increasing the salinity decreases the head-water interaction, thus increasing R and the hydrophobicity of the surfactant system. Due to that increase, R and emulsions transition from one type to another.

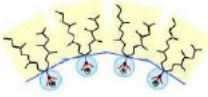
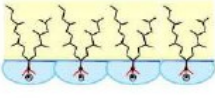
Another criterion in emulsion description is their interfacial film's curvature. This curvature is dependent on the surfactant's head shielding effect:

- Slight shielding → repulsion of heads → oil in water emulsion
- Strong shielding → attraction of heads → water in oil emulsion

Table 2 relates the Winsor ratios with Winsor emulsion types and curvature shape (Buijse et al., 2012 [5])

Table 2. Winsor Classification

Winsor Ratio	Winsor Type	Microemulsion Type	Curvature	Notes
R<1	I	Oil in water (O/W)	<p><u>WR < 1: Under-optimum</u></p>  <p>Low salinity • Little shielding of head-charges • Large head-head repulsion • Oil-in-water emulsion</p>	<ul style="list-style-type: none"> • Excess oil phase • Oil in the middle of micelle • Under optimum • Low salinity environments • Strong head-brine interaction

R>1	II	Water in oil (W/O)	<p><u>WR > 1: Over-optimum</u></p>  <p><u>High salinity</u></p> <ul style="list-style-type: none"> • Excessive shielding of head-charges • Small head-head repulsion • WR > 1, water-in-oil emulsion 	<ul style="list-style-type: none"> • Excess water phase • Water in the middle of the micelle • Strongly hydrophobic surfactant • Over optimum • High salinity environments • Strong tail-oil interaction
R=1	III	Co-existence of 3 separate phases: oil, water, and microemulsion	<p><u>WR = 1: Optimum</u></p>  <p><u>Optimum salinity</u></p> <ul style="list-style-type: none"> • Head and tail same size • Zero effective curvature • micro-emulsion 	<ul style="list-style-type: none"> • Optimum case • Balanced interactions • Preferred for EOR applications because they provide: <ol style="list-style-type: none"> a. lowest IFT b. high capillary number c. high displacement efficiency
	IV	One homogeneous single-phase microemulsion system		These microemulsions are an extension of type III. A continuous increase of surfactant concentration forms them.

2.3 Emulsions

2.3.1 General definition

Emulsions are systems of a minimum of two immiscible liquid phases where one phase is dispersed in the other (Lim et al., 2015 [19]). Mainly emulsions can be divided into two types: microemulsions and macroemulsions. The main differences are that the microemulsion has a droplet size of 1 to 100 nm and is thermodynamically stable. In contrast, the macroemulsion has a droplet size larger than 100 nm and is thermodynamically unstable (Liu et al., 2019 [20]).

Microemulsions can be formed spontaneously through ultralow IFT surfactant flooding, where they will affect the displacement dynamics. Moreover, as discussed previously, emulsions also follow the Winsor classification of oil in water, water in oil, or microemulsion system.

2.3.2 Effect on displacement and recovery: Emulsification

Since surfactants and alkaline behave similarly, their role in oil recovery will be discussed conjointly. As discussed briefly previously, surfactants generally affect oil recovery by four mechanisms: IFT reduction, wettability alteration, foam generation, and emulsification.

Emulsification is the process of forming emulsions. Emulsification affects the displacement process and recovery by two mechanisms: emulsification and entrainment and emulsification and entrapment.

2.3.2.1 Emulsification and entrainment:

A significant reduction in IFT allows the oil to emulsify in the water phase. This usually happens when the formed emulsions' sizes are equal to or less than pore sizes. In that case, the oil can be swept out and produced.

2.3.2.2 Emulsification and entrapment:

As the name suggests, this mechanism happens when the IFT is not low enough to make the emulsions droplets smaller, so they get trapped in the smaller pore throats. This allows the surfactant solution to be diverted to un-swept areas increasing areal and vertical sweep efficiencies. This mechanism is mainly used in the production of viscous oils (Johnson, 1976 [14]).

These mechanisms have been proven to increase oil recovery. According to Zhou et al., 2018 [36], when the surfactant was better emulsified, recovery was enhanced by 9.84%.

2.3.2.3 Achieving Emulsification:

To achieve emulsification and disperse one fluid into a continuous phase, a large amount of mechanical energy is needed as well as the satisfaction of three conditions (Akbari and Nour, 2018 [2]):

- a. Immiscibility between the emulsion phases
- b. Agitation for dispersion
- c. Presence of surfactants

Different factors like temperature, time, and pressure lead the emulsions to change their shape, size, and stability throughout their life cycle. Some examples of emulsion formation include, but are not limited to, shaking, mixing, or injecting liquid through porous membranes, i.e., Membrane emulsification (Akbari and Nour, 2018 [2]). Membrane emulsification uses a

membrane that resembles pore throat structures to produce emulsion droplets, as seen in Figure 5. The membrane pore size controls the emulsion droplet size. This technique allows emulsification without great mechanical stress.

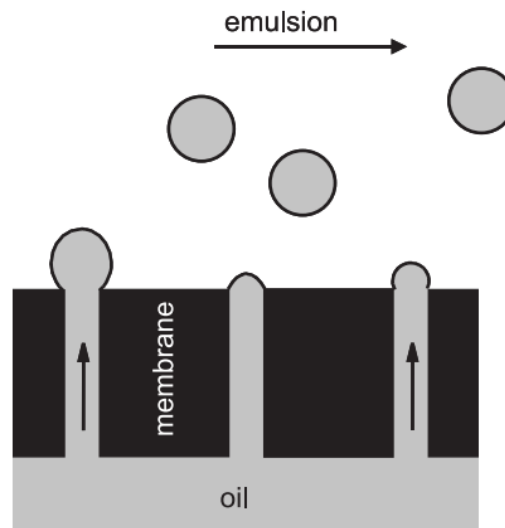


Figure 5. Membrane Emulsification. (Akbari and Nour, 2018 [2])

In general, the size of the emulsion or droplet is affected by the three parameters (Garstecki et al., 2004 [7]):

- The flow parameters of the two phases
- The fluid characteristics of the two phases
- The geometrical factors of the network structure

This thesis expands on the theory of membrane emulsification to see whether this mechanism can also occur in the reservoir and studies each other parameters mentioned above. The question it serves to answer is: How does changing the fluid injection rate, pore structure characteristics, and injected fluid type affect emulsification and fluid displacement?

2.4 Micromodels

Micromodels can be used to understand the influence of emulsions and pore structure on fluid displacement. They are generally made of two transparent plates, like glass for this thesis, with a pore structure etched on one of these plates. The sizes and depths of the pore structures are adjustable depending on each experiment's objectives. Such set-ups are known as Lab on a Chip (LOC). LOC allows the visualization of fluid interfaces and emulsion formation more precisely

with respect to different pore structures. Thus, they serve as a simplified porous network that allows detailed observation of emulsion flow with less injection volume required, a faster time, and lower cost (Zhang et al., 2016 [35]).

Our use of LOCs is to examine the effect of different pore structures and injected fluid types on emulsion formation and first contact displacement.

Several papers include the investigation of the influence of structure geometry on droplet formation and emulsification. Below are some of these studies and the results they achieved:

2.4.1 Waterflooding and aspect ratio (Pradhan et al., 2018 [24])

This study involves microfluidic experiments to comprehend the influences that aspect ratio (AR) and wettability have on residual oil saturation (S_{or}) in waterflooding. While reservoir scale sweep efficiency is influenced by gravity override, viscous fingering, and thief zones, pore-scale displacement efficiency, on the other hand, is affected by wettability and pore-to-throat aspect ratio.

Similar to this thesis, the microfluidic chips included linear pore networks with a depth of 20 μm and various ARs, as seen in Figure 6. The aqueous and oil phases were water and n-decane, respectively. The waterflooding injection rate was 0.1 $\mu\text{l}/\text{min}$ (0.006ml/h) to maintain capillary numbers inside a range of 10^{-7} to 10^{-5} to meet reservoir values. A constant back pressure of 100 psig was maintained throughout the experiments. ImageJ software was used to measure the residual saturations.

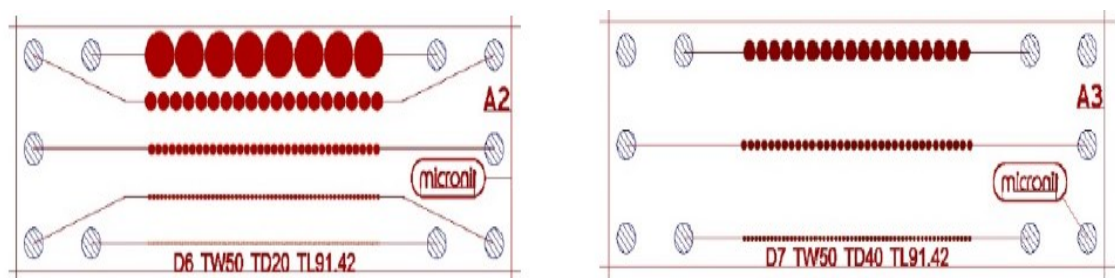


Figure 6. Design of linear pore networks. (Pradhan et al., 2018 [24])

As seen in Figure 7, their results showed that S_{or} increases with AR on a semi-log scale for both hydrophobic and hydrophilic chips. To understand the reason behind this relationship, the capillary number (N_{ca}) was calculated. By comparing AR vs. S_{or} and N_{ca} vs. S_{or} (Figure 7), they hypothesized that the increase in S_{or} with higher ARs may be caused by the decrease in the displacing fluid velocity in the larger pores.

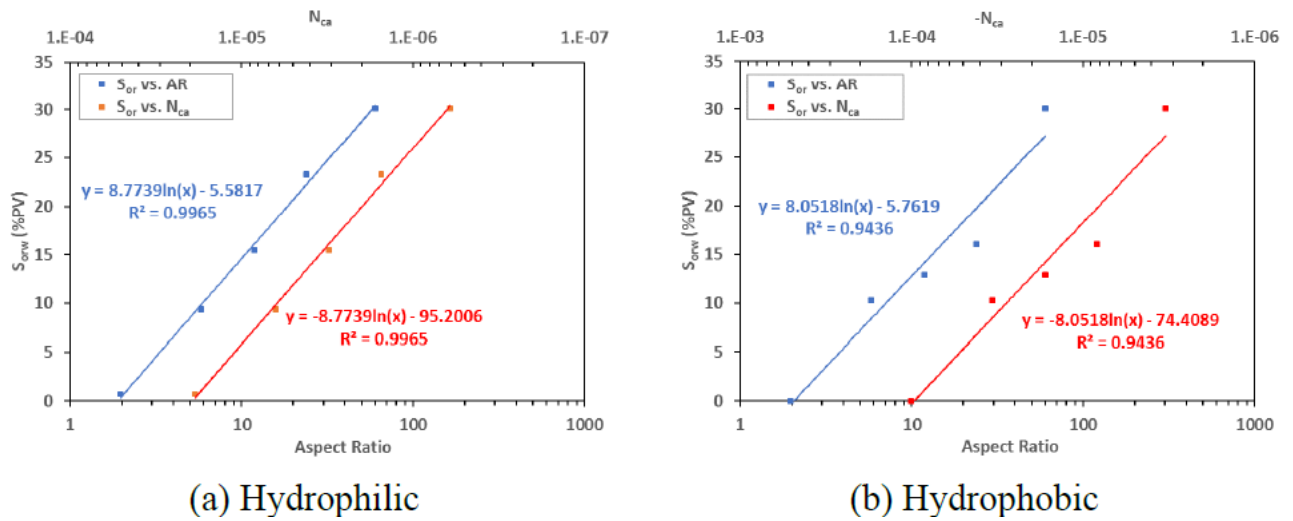


Figure 7. Effect of AR and Nca vs Sor. (Pradhan et al., 2018 [24])

2.4.2 Development of foam-like emulsion phases in porous media flow (Kharrat et al., 2022 [16])

Their microfluidics experiments revolved around investigating emulsification and miscibility with surfactant flooding. They varied the salinity (NaCl concentration) across optimal displacement conditions from 1 to 5 wt%, and studied the resulting emulsion textures.

Their first step was to have a clear idea of the fluid-fluid interaction. Spinning drop IFT results were misleading in representing the initial two-phase system because they produced emulsions and phase separation in all cases. Hence, they went for test-tubes experiments.

- Test-tube experiments:

Equal volumes of 5ml of oil and surfactant solutions were injected into glass test tubes. Then, the fluids were mixed using a tube rotator and placed vertically to reach gravity-separated phases. Figure 8 represents the final equilibrium states, where at 2wt% and 2.5wt% both the upper and lower phases are relatively clear and the behavior changes from a lower slightly blurred phase to a higher slightly blurred one. This indicates that these are the (near) optimum conditions. For that reason, this thesis will use the 2wt% surfactant cocktail as near-optimum case, and the 4wt% one as over-optimum.

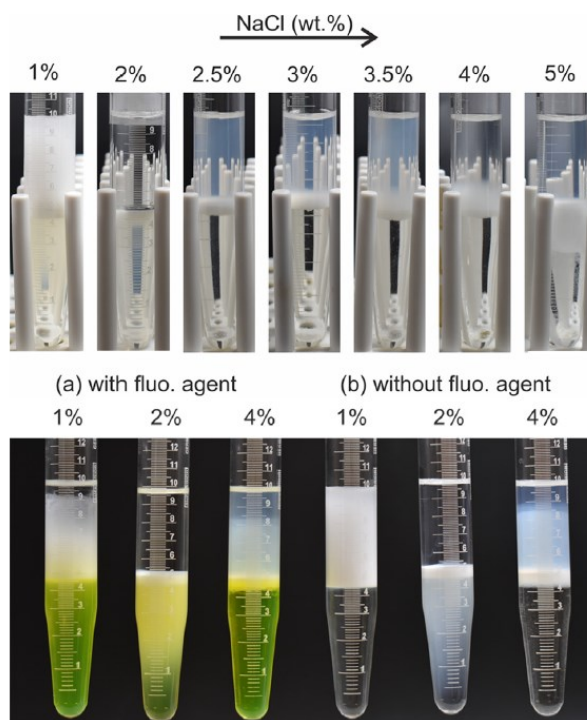


Figure 8. Test-tube phase behavior experiments of a decane-surfactant solution system with increasing NaCl, top: experiment without contrast agents, bottom: simultaneous experiments (a) with and (b) without fluorescence contrast agent. (Kharrat et al., 2022 [16])

- Nano structures of emulsion phases

In the above experiments, phases were observed to be milky or transparent. A transparent phase may be indicative of a pure fluid phase or might include microemulsions that are invisible to the human eye because they have a particle size less than the wavelength of light. In order to see if the transparent and milky phases contain microemulsions, they used small-angle X-ray scattering (SAXS) to visualize nm-size particles (Figure 9). They repeated the previously mentioned experiments using Mark tubes to suppress gravity segregation. Their results showed that in both cases, the microemulsion exists. However, in the milky phase, other textures, such as macroemulsion, can be assumed as it is not transparent.

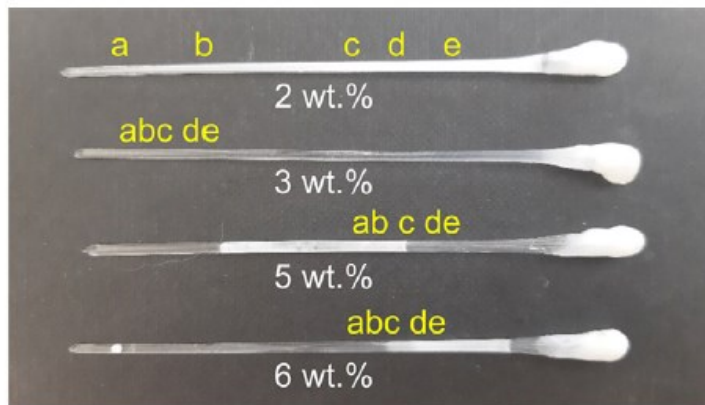


Figure 9. Smallscale test tubes with indicated NaCl concentration and positions at which SAXS measurements were taken. (Kharrat et al., 2022 [16])

- Flooding experiments

As previously mentioned, they investigated displacement and emulsion development during surfactant flooding. Across all the experiments, foam-like emulsion phases with different qualities and transport properties were observed. Contrary to classical foam flooding, the displaced phase (oil) was getting solubilized, mobilized, and participating in the resulting mixed phase.

As for displacement, three mechanisms were seen. The first was the drainage of oil through the thinning of the oil films leading to the increase in foam quality (Figure 10). The second is oil displacement as a solubilized phase in the injected water, which is compartmentalized in the foam structure. The last mechanism was the production of oil from dead-end pores.

(a) film and lamella thinning by drainage

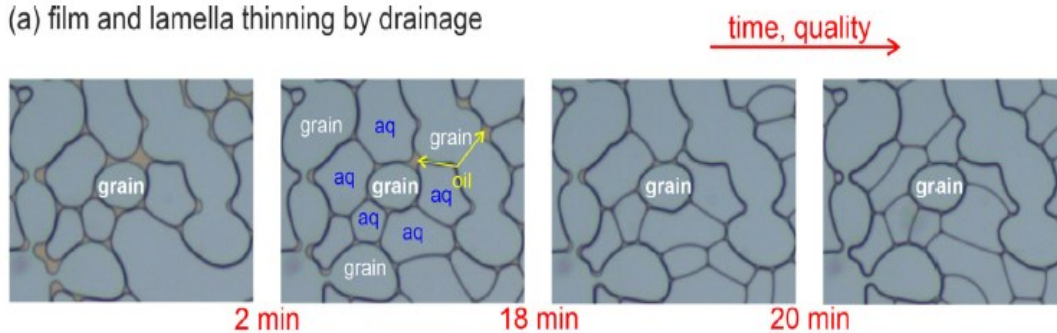


Figure 10. One of oil mobilization mechanisms: Film thinning and drainage process. (Kharrat et al., 2022 [16])

The main difference between near and over optimum behavior is the degree of oil solubilization. At near optimum conditions, stronger solubilization occurs where foam-like structures transition into a single fluid phase. On the other hand, at over optimum conditions, foam-like phases are constrained to the displacement front.

As discussed previously, this thesis will be studying emulsification and fluid displacement by not only altering the fluids in place and injected in terms of surfactant and alkaline concentrations, type of oil in place, and injected fluid velocity, but by also changing the pore network characteristics in terms of aspect ratio, pore bodies and throats sizes, and distance between the pores.

Chapter 3

Experimental Equipment

3.1 Porous Medium

Microfluidic chips, which represent a 2D porous medium, were used for the experiments. These chips are made of borosilicate glass. The pattern consists of a homogeneous etching depth of $20\ \mu\text{m}$ and a lateral definition of pores and pore throats. Five different chip designs were used in the experiments. The dimensions of each chip are shown in Table 3. In addition, an illustration of these dimensions can be seen in Figure 11, where λ represents the distance between the pores, **Pb** is the diameter of the pore body, **Pt** is the diameter of the pore throat, and **Aspect ratio (AR)** is defined as the ratio of **Pb** to **Pt**.

Table 3. Microfluidic chips design.

Distance between pores λ (μm)	Pb (μm)	Pt (μm)	AR
100	160	50	3.2
100	155.4	96.7	1.6
100	226.9	50.9	4.5
500	406.9	50.9	8.0
2500	408.9	51.5	8.0

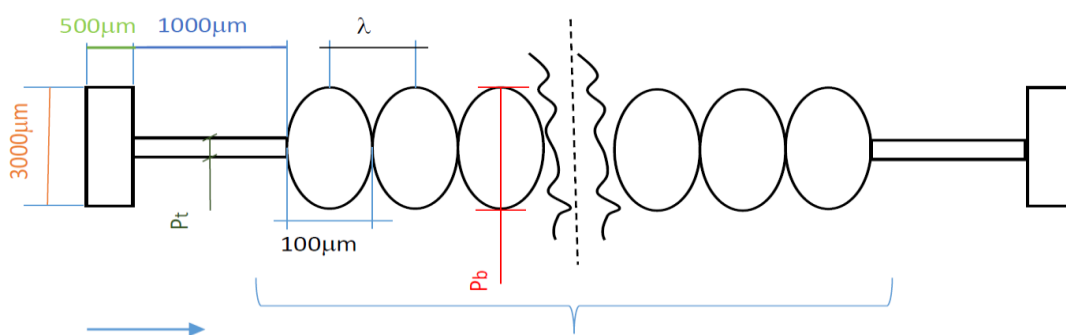


Figure 11. Illustration of chip dimensions.

Figure 12 and Figure 13 show the actual chips representing the porous media for all the different dimensions.

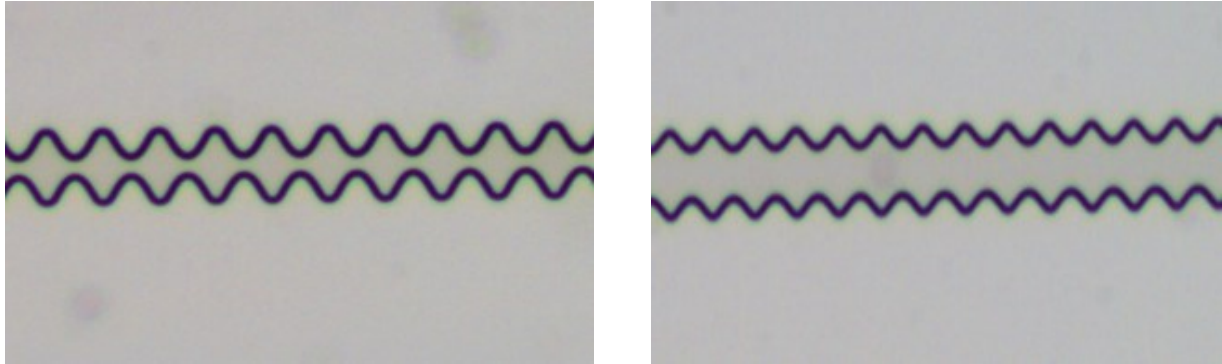


Figure 12. Empty pore systems, left: AR 3.2, $\lambda=100 \mu\text{m}$, right: AR 1.6, $\lambda=100 \mu\text{m}$.

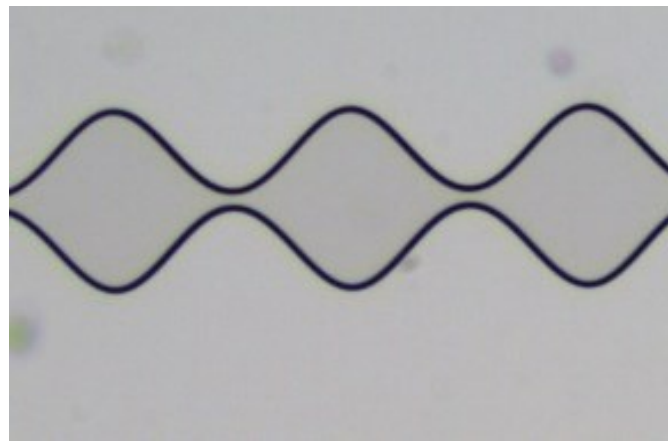


Figure 13. Empty pore system, AR 8 $\lambda=500 \mu\text{m}$

3.2 Instrumentation

The experimental setup and instrumentation used were like the ones used in Kharrat et al., 2022 [16]. The experiments were performed at ambient conditions with a constant pressure boundary condition at the outlet. This constant pressure boundary condition was achieved by producing the fluids into a container subjected to atmospheric pressure. A high-precision Chemyx Fusion 200 syringe pump was used to inject the fluids. A distinct syringe was used for each fluid type. Detailed and high-quality optical images of the pore space and the fluids within were captured using a Leica DMI8 microscope. A wide range automated XY table was used with image stitching software to image the pore space. A Leica DMC2900 camera was used to record these images with a pixel size of $1.8 \mu\text{m}$. In addition, videos were captured of smaller regions that were particularly interesting. A vacuum pump was also connected on the downstream side to

prepare the setup by emptying the pore space and the flow lines and pre-saturating them (Kharrat et al., 2022 [16]).

3.3 Fluids

Two sets of fluids were used for the experiments. The first set consisted of using decane as the oil phase. Deionized water (DI) was used as the injected water. Additionally, a surfactant cocktail similar to the one used in Kharrat et al., 2022 [16]. J13131 (C12-C13 alcohol alkoxy sulfate, 13 PO) was used as a surfactant, 2-butanol as a co-solvent, and varying sodium chloride (NaCl) concentrations as a tuning factor. NaCl concentrations of 2 wt% and 4 wt% were used because they represent near optimum and over optimum conditions, respectively, as discussed in the work of Kharrat et al., 2022 [16]. Contrast agents were also needed to create optical contrast because both decane and water are clear fluids and optically identical. That's why Sudan II was added to the oil phase as a colorant, which turned the oil phase into a brownish color. The effect of this colorant on the IFT and phase behaviour was studied in Kharrat et al., 2022 [16], and no considerable impact was seen (Kharrat et al., 2022 [16]). The first set of fluids and chemicals can be seen in Table 4. Fluids used

Table 4. Fluids used

Chemical	Concentration	Source
J13131	0.5 wt %	Shell
2-Butanol	2 wt%	Sigma Aldrich
NaCl	2 and 4 wt%	Sigma Aldrich
Sudan II	10 mg/l	Sigma Aldrich

The second set of fluids used were similar to the ones used in Borji et al., 2022 [4]. An oil sample, referred to as Oil 16th, obtained from the Vienna basin was used as the oil phase. The properties of Oil 16 can be seen in Table 5. DI water was used as the injection water. The injected fluid consisted of alkaline solutions prepared with DI and Na_2CO_3 as an alkali agent with two concentrations, 3000 and 7500 ppm. These concentrations were used because 3000 ppm represents the under optimum condition and 7000 ppm represents the optimum condition, as discussed in the work of Borji et al., 2022 [4].

Table 5. Oil 16 properties.

Property	Value
Viscosity at 20°C	330 cP
Interfacial Tension (IFT) to water at 20°C	0.7 ±0.1 mN/m
Total Acid Number (TAN)	1.96 mg KOH/g oil

Additional fluids were used to clean the chips before each experiment. These fluids were mainly distilled water, acetone, and toluene.

Chapter 4

Experimental Procedure

4.1 Cleaning Procedure

Prior to any experiment, the microfluidic chips were cleaned by injecting a series of solvents. For the first set of fluids, water and decane were used for flushing the chips to remove any remaining surfactant, salt, and dye agents. Then, acetone was injected to flush any remaining fluids. Finally, the acetone was vaporized from the system by injecting air and applying the vacuum for several hours.

For the second set of fluids, the cleaning procedure was as follows. First, 250 pore volumes (PVs) of distilled water were injected at different flow rates. After that, acetone and toluene were injected at low flow rates to ensure efficient mixing and displacement of the fluids within. The sequence was as follows: 50 PVs of acetone were injected followed by 50 PVs of toluene, then another 50 PVs of acetone followed to remove the toluene. Finally, the acetone was vaporized by injecting air and applying the vacuum.

The cleaning process was observed with a microscope to ensure its effectiveness and quality.

4.2 Experimental Procedure

The experiments were conducted at ambient conditions with a constant pressure boundary condition at the outlet and a constant flow rate boundary condition at the inlet. The initial state of the porous domain in all experiments was fully saturated with the oil phase (Oil 16 or Decane), $S_{o,initial} = 1$. Then, the solutions (surfactant cocktail or alkaline solutions) were injected with an injection rate of 0.0008 ml/h refer as low injection rate, which corresponds to a Darcy velocity of 1 ft/day on a reservoir scale. Another set of experiments used an injection rate of 0.005 ml/h refer as high injection rate for comparison. When changes in oil saturation

could no longer be seen, the experiments were ended. Optical images were taken of the porous domain as mentioned before. These images were taken mostly with a small field of view that covered the total domain after stitching. Thus, emulsification and displacement processes could be observed on a sub-pore scale due to the high spatial resolution provided by this small field of view.

4.3 Calculations

1. Average remaining oil saturation (Avg ROS) with first contact displacement (4.2):

ROS in each pore (ROSp) (4.1):

$$ROSp (\%) = \frac{\text{Area of oil left in pore}}{\text{Area of entire pore}} \times 100$$

4.1

$$Avg ROS (\%) = \frac{ROSp}{\text{number of pores}}$$

4.2

The area of the oil left in each pore and the area of the entire pore were acquired in pixels with the Image J software, as seen in Figure 14. The number of pores was generally between 4 to 8, depending on whether the amount of oil left was constant or changing from one pore to another.

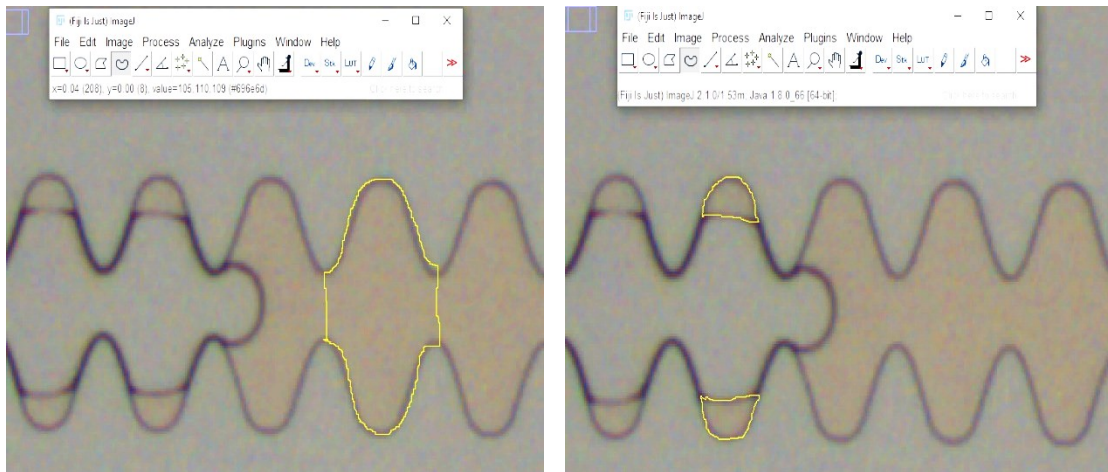


Figure 14. Area of entire oil filled pore (left), area of oil left in pore (right).

2. Velocity:

$$Velocity (\mu m/s) = \frac{Distance(\mu m)}{Time(s)} \quad 4.3$$

$$Time (s) = \text{time position} \times \text{time interval (s)} \quad 4.4$$

The velocity calculated is the first contact in-situ front velocity (4.3). An image sequence of the displacement process recorded with the microscope is imported through the Image J software. The distance is measured from the center of the front from time 0 until time x (when the front is at time position x), as seen in Figure 15.

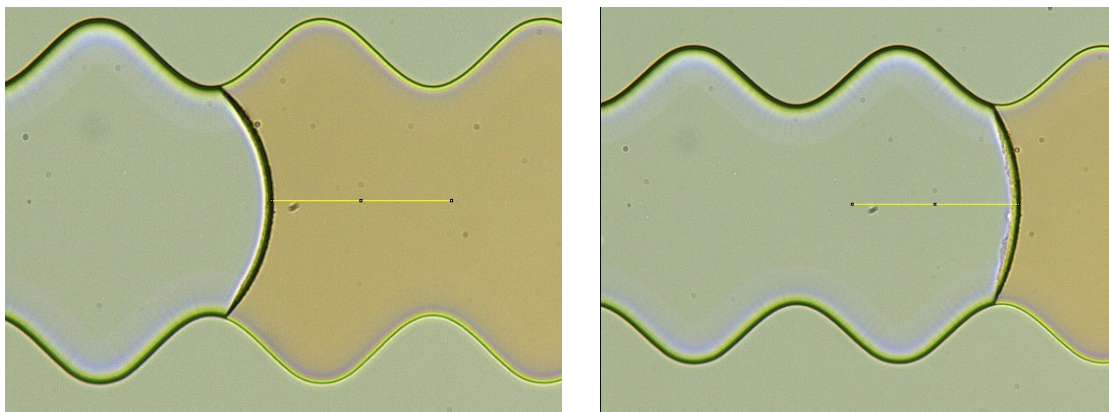


Figure 15. Distance measurement from position 0 till position x.

Velocities wrt previous (m/s) were calculated by taking the distance from time x till time x+1 and dividing by the time interval between them.

3. Recovery factor (RF):

$$RF(\%) = \frac{Produced\ Oil}{Initial\ oil\ in\ place} \times 100 \quad 4.5$$

The produced oil is calculated by subtracting the final oil in the system from the initial oil-filled pore space (4.5). The final and initial oil quantities are measured in pixels differentiated with color thresholds using the Image J software.

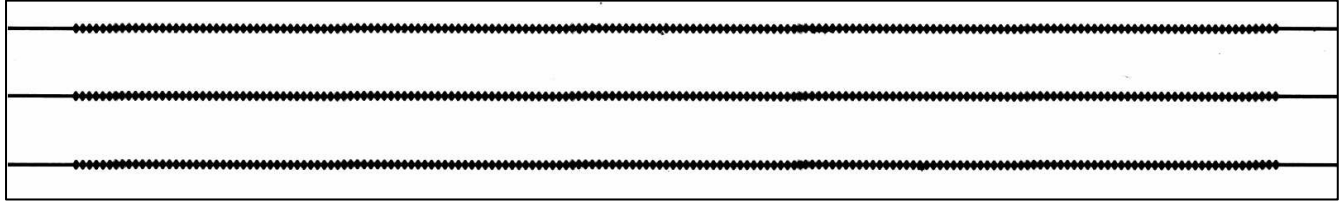


Figure 16. Oil filled pore system in binary using Image J.

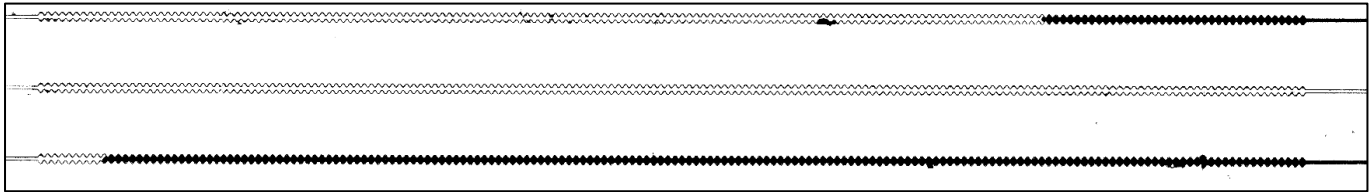


Figure 17. Oil left at final stage in binary using Image J.

4. Reynold's Number (Re) (4.6):

$$Re = \frac{\rho \times v \times r}{\mu}$$

4.6

Where: ρ = injected phase density (kg/m³), v = Velocity wrt previous (m/s), r =radius (m)=Pb or Pt, μ = injected phase viscosity (Pa.s) (values taken from Table 6).

Table 6. Injected fluid properties

Injected	Density (kg/m ³)	Viscosity (Pa.s)
DI	1000	0.001
2% surfactant	1019.6	0.001

Chapter 5

Results & Discussion

Note: emulsions in this chapter refer to everything with a bubble shape or even droplets that can be resolved by microscope images or visible with the naked eye. Hence, dots and bubbles are considered emulsions. Microemulsions may occur especially in the near-optimum (Kharrat et al., 2022 [16]). However, these were not visible and thus are not included in our emulsion definition of first contact displacement.

Several factors are considered to study and describe the displacement process and efficiency. These are the front shape, amount of trapped oil either at a final stage for recovery factor or at a breakthrough phase for first contact remaining oil analysis, and emulsion formation at the initial breakthrough stage and their development with time. Changing the oil in place, injected fluid, injection rate, and geometrical characteristics of the pore space allow us to examine the possible direct or indirect relationships between these displacement and experimental factors. All these factors are described during first contact displacement unless stated otherwise.

Note: An error bar was used to portray results representing image analysis errors.

5.1 Reynold's Number:

As discussed in Chapter 2, emulsion formation is influenced by flow characteristics. Turbulent flow enhances mixing and agitation and thus can be a possible reason for emulsion formation. To check if the emulsions seen in our generic fluids experiments are caused by turbulence, Reynold's Number (Re) is calculated. Re is the go-to method to determine the flow regime, where turbulence is characterized by $Re > \sim 2000$ (Yang et al., 2021 [32]).

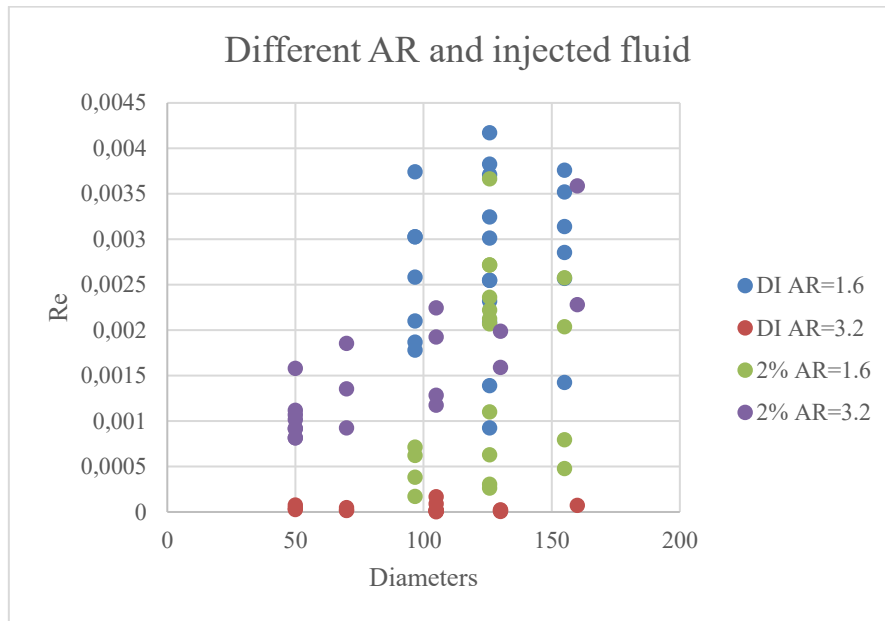


Figure 18. *Re* for water and 2% NaCL surfactant injection for AR 1.6 and 3.2 vs pore diameters (radii).

As seen in Figure 18, although ranges differ due to differences in velocities and diameters, the values are very small to indicate turbulent flow. This may be due to the incredibly small diameter values (μm). So, we assume that any emulsions formed are not due to *Re* and turbulence.

5.2 Generic fluids — Different ARs, $\lambda=100 \mu\text{m}$, Low Injection rate (0.0008 ml/h)

5.2.1 First contact displacement and emulsion characterization

DI Injection

During DI injection in all ARs, the breakthrough occurred in one channel, and the other two remain unswept. In these cases, the final RF is used to quantify displacement efficiency. As expected, no emulsions were produced during these experiments. First contact displacement for all three ARs is shown in Figure 19Figure 20Figure 21.

Table 7. Same distance between pores ($\lambda=100 \mu\text{m}$) and different AR

	AR=1.6	AR=3.2	AR=4.5
Front shape	Concave	Concave	Concave
Trapped oil	Yes	Yes	Yes
RF (%)	54	59	38

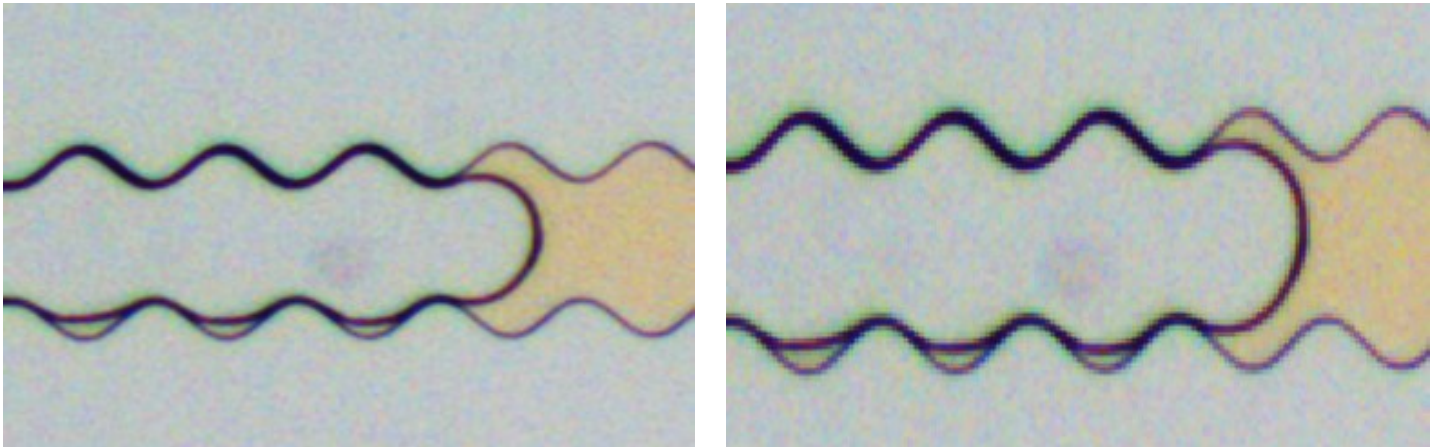


Figure 19. Concave front and remaining oil for AR 1.6. Pictures are 1 second apart.

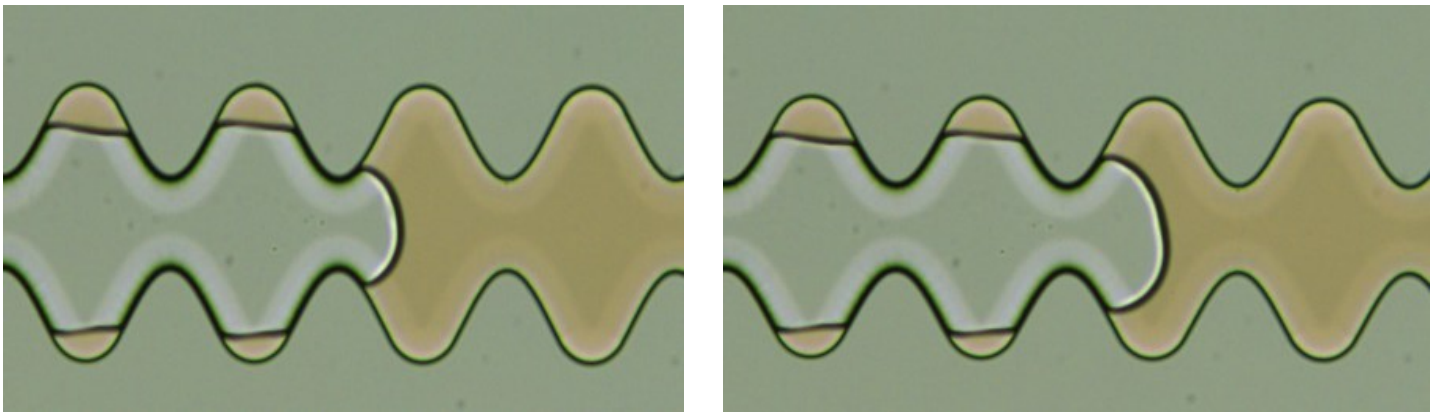


Figure 20. Concave front and remaining oil for AR 3.2. Pictures are 0.5 second apart.

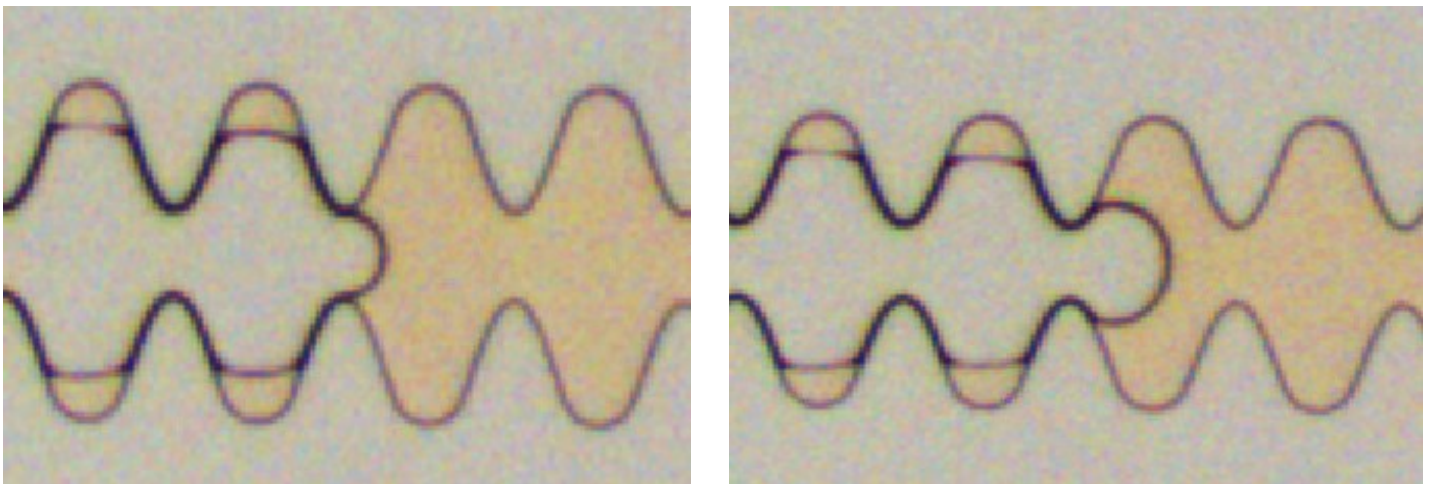


Figure 21. Concave front and remaining oil for AR 4.5 Pictures are 0.5 seconds apart.

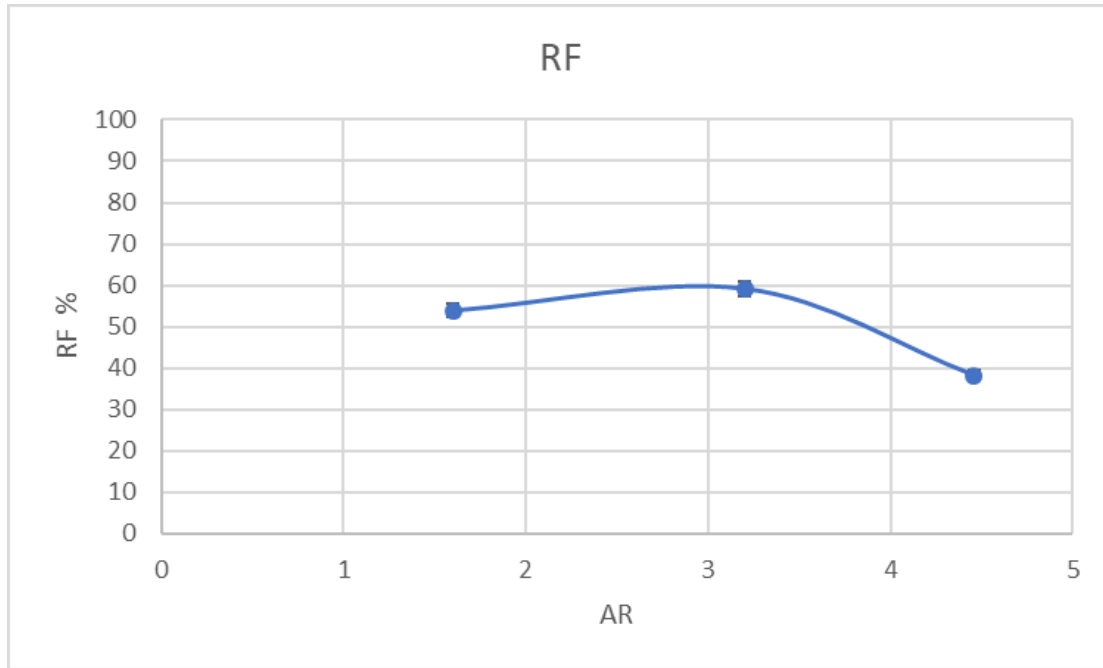


Figure 22. RF vs AR for DI injection

While the initial entrapment of oil is visible along all ARs, the final RF differs (Figure 22 and Table 7). Hence, we can assume that AR affects recovery efficiency. The difference in RF is attributed to how much DI was able to displace oil in the three channels before BT. As seen in Figure 23, for ARs 1.6 and 3.2, almost significant oil displacement occurred in two channels with bypassing of only one channel. In contrast, for AR 4.5, oil was swept mainly in one channel.

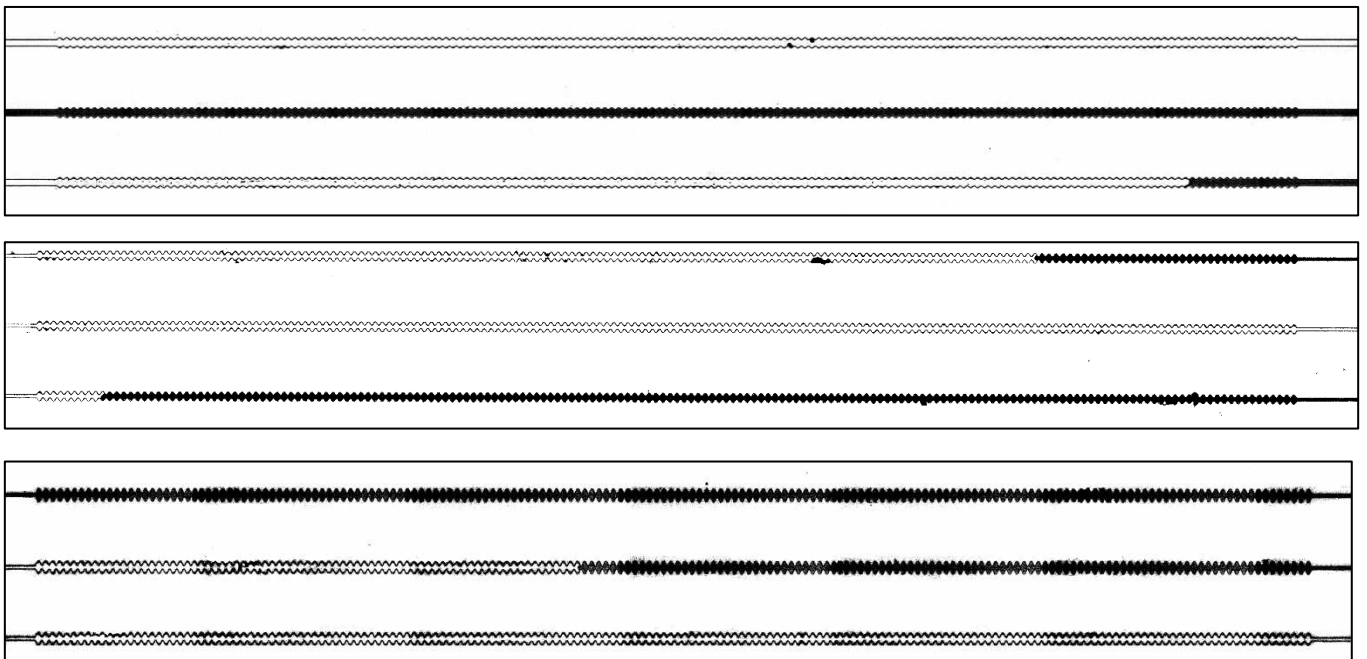


Figure 23. Final images in binary. Top: AR 1.6, middle: AR 3.2, bottom: AR 4.5. Almost complete bypass of 2 channels for AR 1.6 and 3.2. less bypass for AR 4.5

Surfactant Injection

When describing emulsions, two terms can be used. The first is solubility. Emulsions are described as soluble when there is a high degree of mixing of the phases where an almost single phase is present. This occurs because emulsions coalesce with each other as they move from inlet to outlet. The second term is stability. Emulsions are described as stable if they are moving but do not coalesce with each other. The interfaces between the emulsions seem more rigid.

Near-optimum condition:

Table 8. First contact displacement characteristics for 2% NaCl surfactant injection and different ARs

	Same λ (100 μm), different AR		
	AR=1.6	AR=3.2	AR=4.5
Front shape	Alternating concave and convex	Concave	Concave
Trapped oil	No	Yes	Yes
Emulsions	Yes (a few)	No	No

Contrary to what is seen in DI injection, first contact displacement for constant λ reveals different results for AR 1.6 (Table 8). This case has an alternating front with no trapped oil in the pores and is the only case with emulsion formation in the near-optimum case. The observed emulsions were very few and small.

While only in AR=1.6, emulsions were seen with first contact displacement, more emulsions appeared with time after BT in all ARs. the shape, size, and stability of emulsions are changed during the displacement with respect to time.

a. AR=1.6, $\lambda=100 \mu\text{m}$

Initially, the front shape was alternated from concave to convex at specific locations (Figure 24), which will be discussed in the section Velocities.

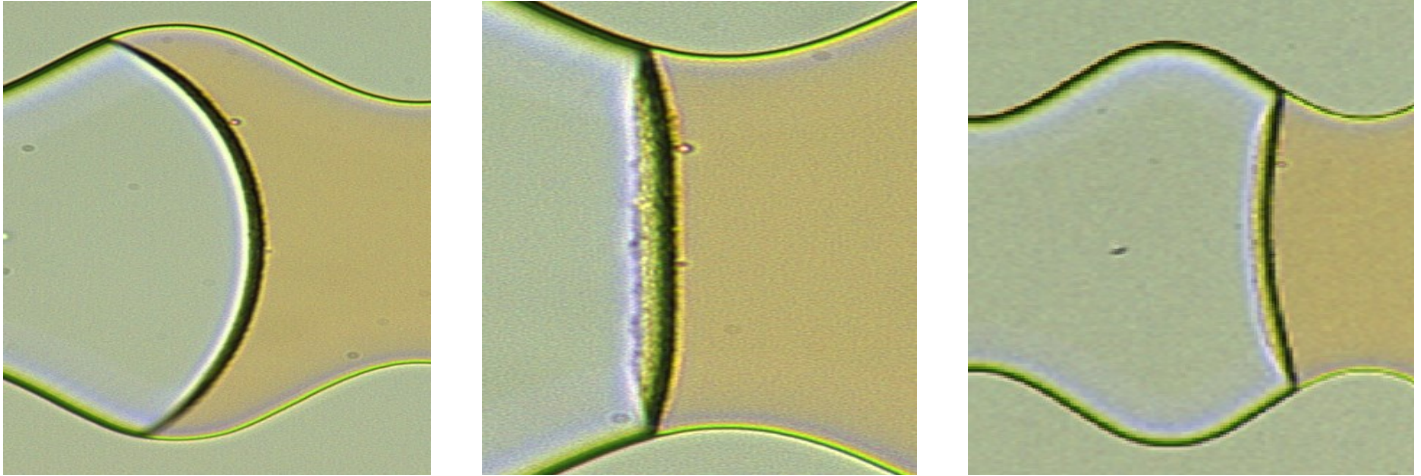


Figure 24. Initial front displacement: Alternating concave to convex with tiny emulsion droplets at the interfaces

As seen in Figure 25, with time, emulsions of different sizes were seen at the surfactant-oil interface. The emulsions flowed along with the oil as it moved towards the pores. Later, there was no clear distinction between the phases as the emulsions were solubilized. Foam-like emulsions can also be seen in Figure 25-top right. The wettability of the pore system remained oil wet as all the oil being produced lay on the pore and throat walls. Figure 25-bottom indicates water in oil emulsions.

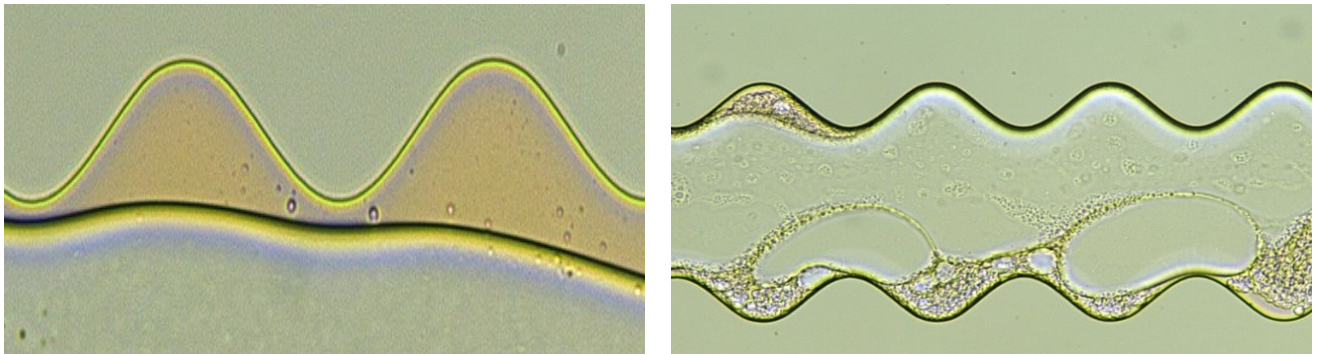


Figure 25. Evolution of the shape of emulsions with time. Top left: tight orange bubbles in the oil phase and at surfactant-oil interface. Top right: loose solubilized foam-like flow. Bottom: final stage of experiment - emulsion with a high degree of solubility

b. $AR=3.2, \lambda=100 \mu\text{m}$

Initially, the surfactant front had a concave shape irrespective of its position throughout the pore system (Figure 26).

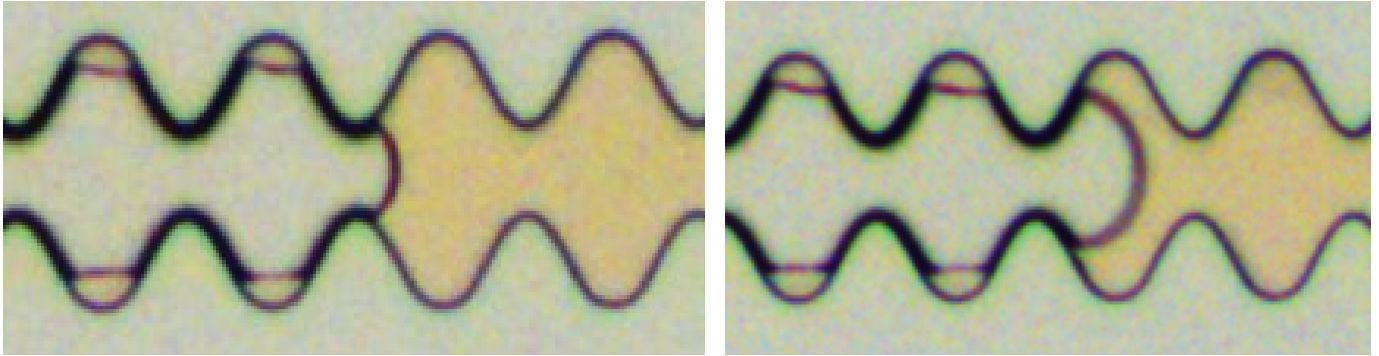


Figure 26. Initial front displacement: Concave front. Time interval between pictures: 40 seconds. the two pictures are not taken at the same location

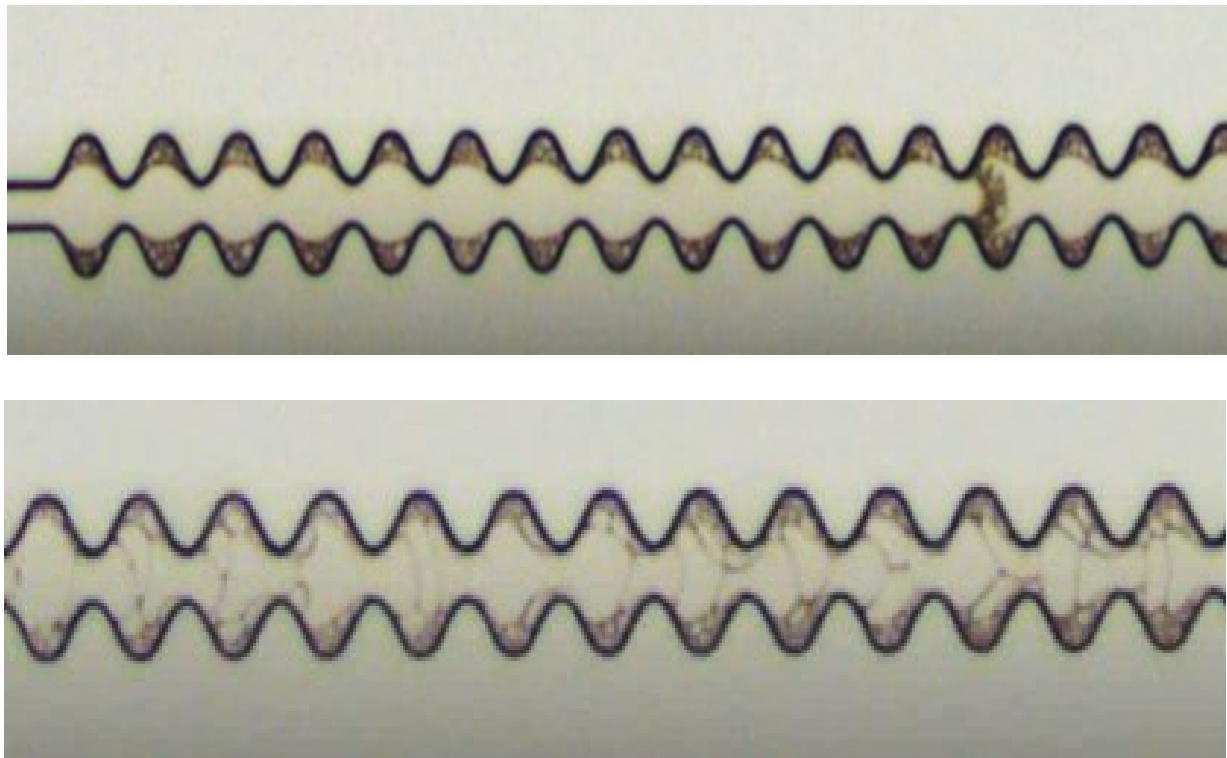


Figure 27. Formed emulsions in bottom channel , which experienced BT first. Top: Five seconds after BT, bottom: 30 seconds after BT.

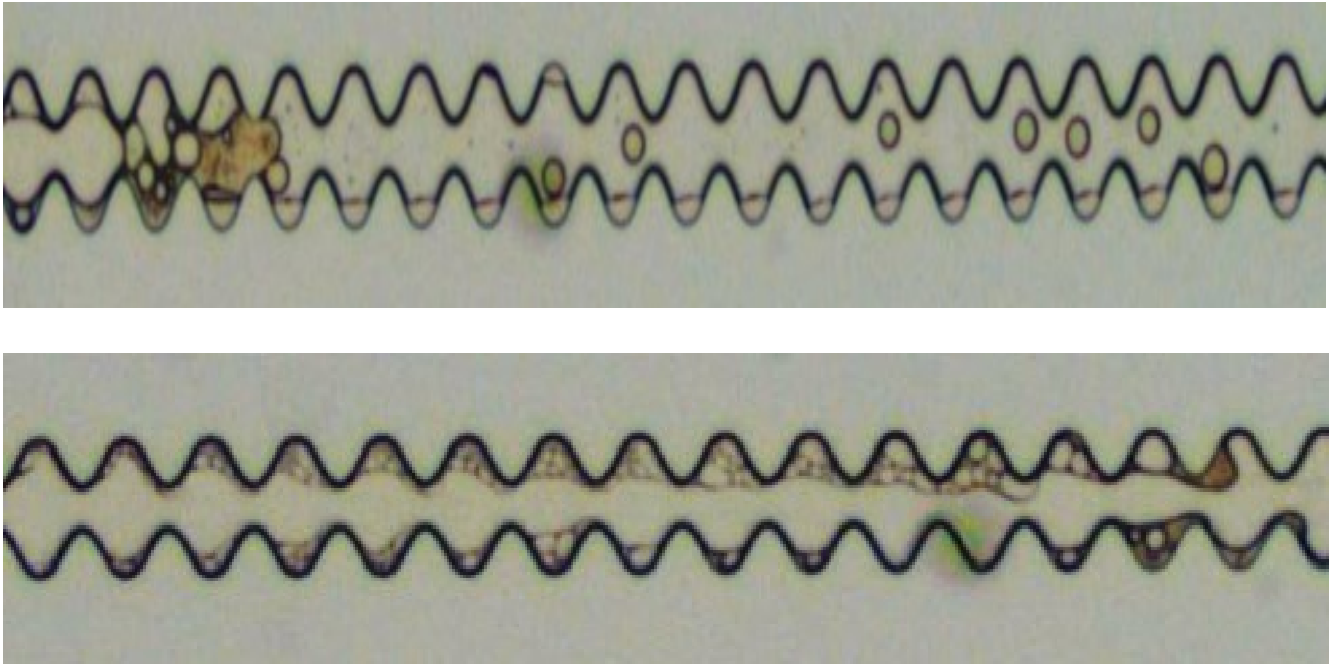


Figure 28. Formed emulsions in top channel , which experienced BT later. Top: Five seconds after BT showing discrete bubbles, bottom: 30 seconds after BT, showing solubilized foam-like emulsion flow.

Figure 26-28 allow us to see how flow and emulsions change with respect to time in different channels. In the bottom channel, the oil was contacted with the surfactant solution earlier than the top channel. The color difference and emulsion types are clearly visible between the channels, where the bottom channel has more of a dark brown color with foam-like emulsions (Figure 27). On the other hand, the top channel has lighter oil present with clear boundaries between the surfactant phase and the oil phase and the emulsions present are rounder, more prominent, and more visible (Figure 28). As time further progressed, the top channel mimicked the behavior of the bottom one.

In general, the flow process looked as follows, as seen in Figure 29 below:

1. Slug flow with a clear distinction between the phases.
2. Foam-like emulsions with more complex structures and a high degree of solubility filling the entire pore space
3. Foam-like emulsions are only attached to the pore cavity's surface.

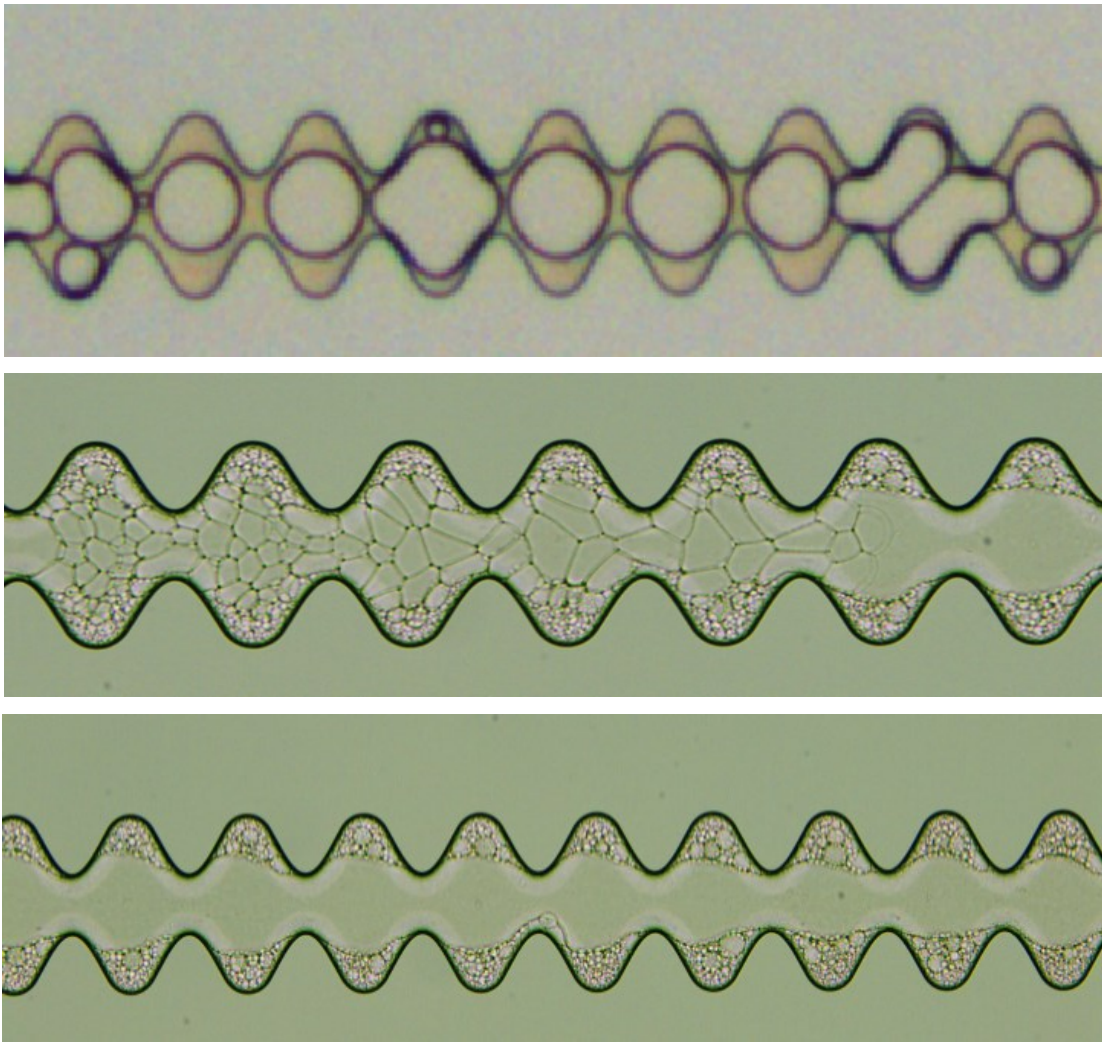


Figure 29. Evolution of flow with time from slug flow to foam-like emulsion flow.

c. AR=4.5, $\lambda=100 \mu\text{m}$

Similar to AR 3.2, the front shape remained concave in AR 4.5 throughout the pore system (Figure 30).

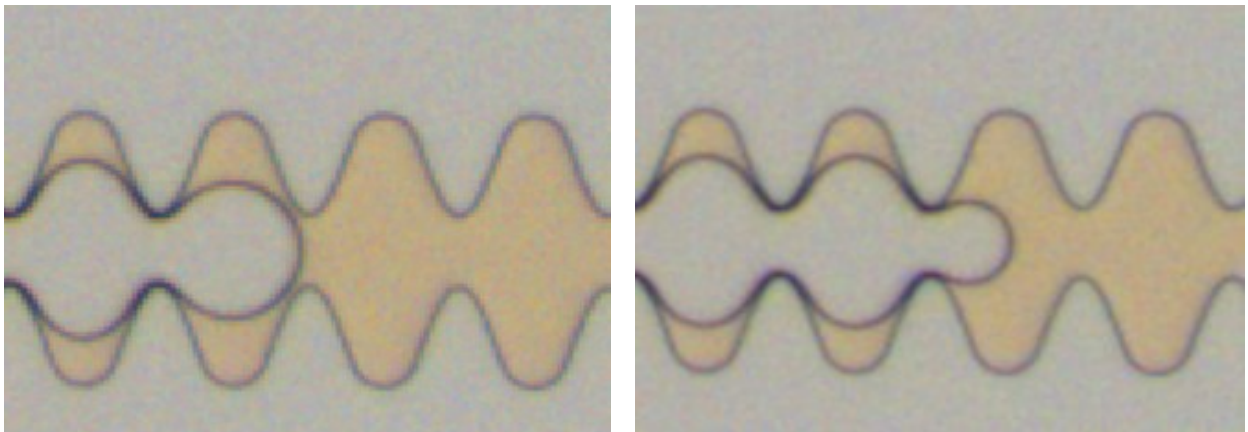


Figure 30. Initial front displacement: Concave front. Time between pictures: 1 second

As further surfactant mixture entered the system, more oil was displaced from the pore cavities due to solubilization (Figure 31 - top). However, bubbles were temporarily stuck in the pore cavities (Figure 31 - middle). Nonetheless, these bubbles and oil in place were displaced, resulting in one phase system (Figure 31 - bottom). Contrary to the two previous ARs, AR 4.5 did not witness any foam-like emulsions.

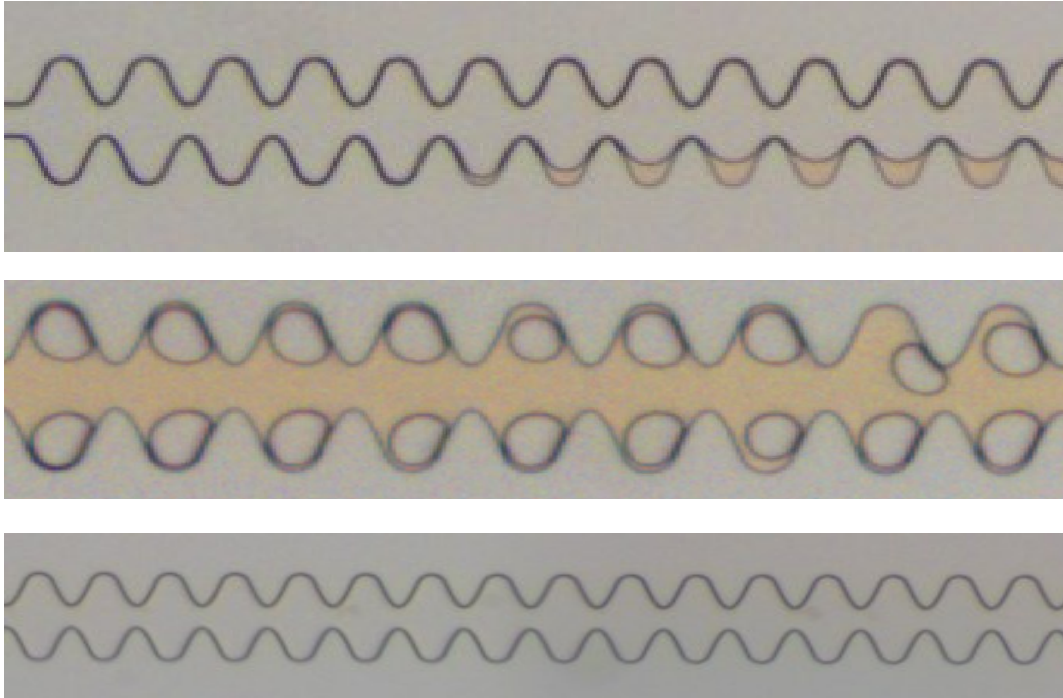


Figure 31. Evolution of flow with. Time is increasing from top picture to bottom one. Complete solubilization achieved.

Over-optimum condition:

Table 9. First contact displacement characteristics comparison for 4% NaCl surfactant solution injection in different ARs.

	Same λ (100 μm), different AR		
	AR=1.6	AR=3.2	AR=4.5
Front shape	Concave to diagonal	Concave	Concave
Trapped oil	No	Yes	Yes
Emulsions	No	Yes	Yes

Similar to 2% injection, front alteration was only seen for AR 1.6. Moreover, the AR 1.6 case did not exhibit any trapped oil or first contact emulsions.

a. $AR=1.6, \lambda=100 \mu\text{m}$

Similarly to how AR 1.6 behaved with the near-optimum condition, a non-constant concave front was observed in this case. The front shape switched from concave to diagonal depending on its position in the pore system (Figure 32).

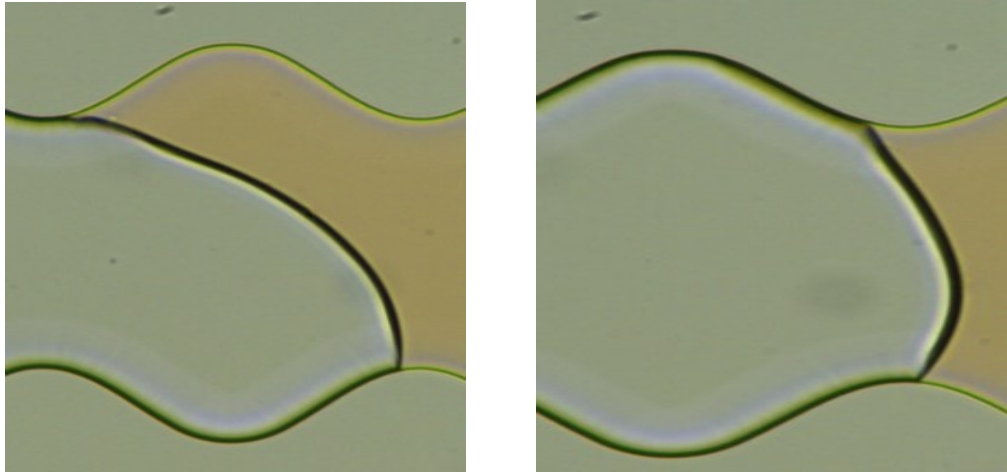


Figure 32. Initial front displacement: Alternating concave to diagonal. Not trapped oil. No emulsions seen.

Even though no emulsions were seen during first contact displacement, some started forming as entrapped phases in the oil (Figure 33, left) or foam-like emulsions (Figure 33, right).

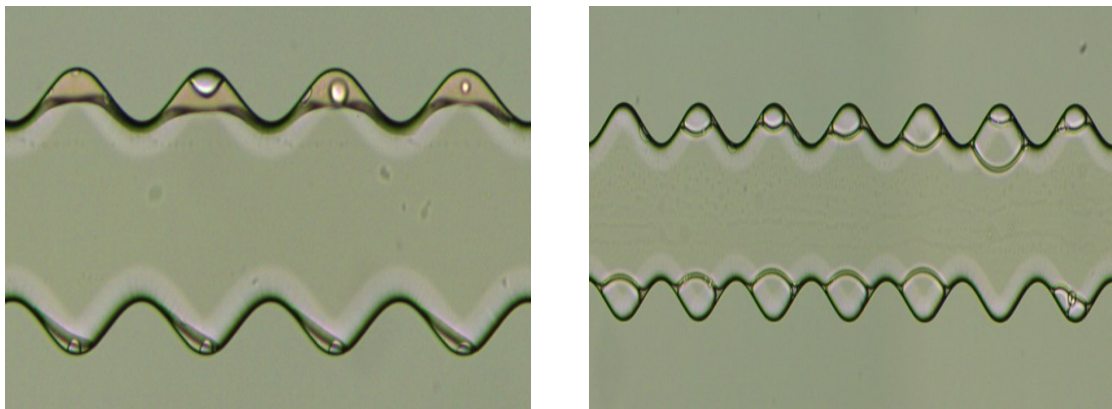


Figure 33. Emulsion formation with time.

b. $AR=3.2, \lambda=100 \mu\text{m}$

Initially, the front remained symmetrical concave irrespective of its position in the pore system. Some emulsion bubbles flowed ahead of the front, and others were stuck at the interface (Figure 34).

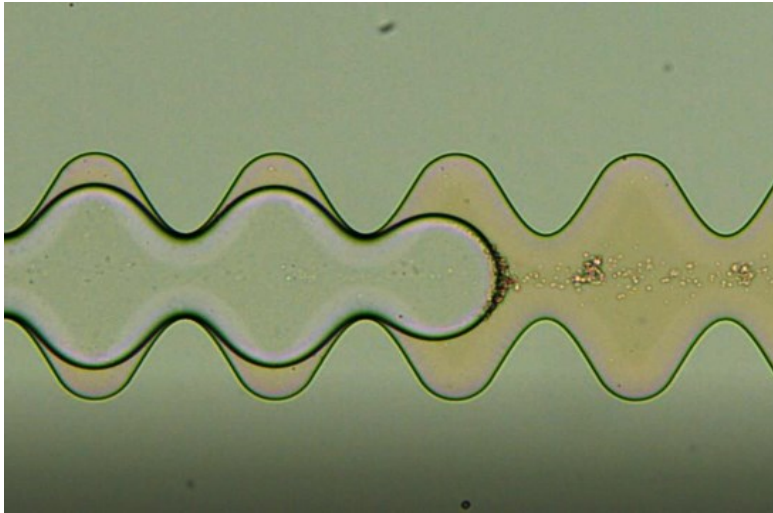


Figure 34. Initial front displacement: remained symmetrical concave with small bubble emulsions

Figure 35 shows displacement started as slug flow coupled with emulsions in the oil phase. As time progressed, the foam-like emulsions formed with rigid surfaces and less solubilization. Finally, the foam-like structures were only stuck to the pore body surfaces and did not interact with the aqueous phase.

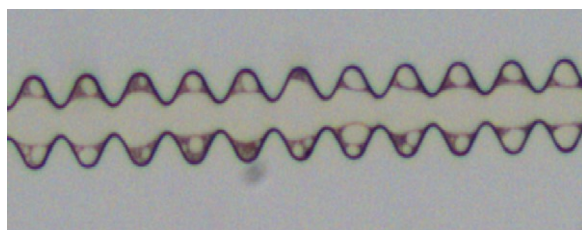
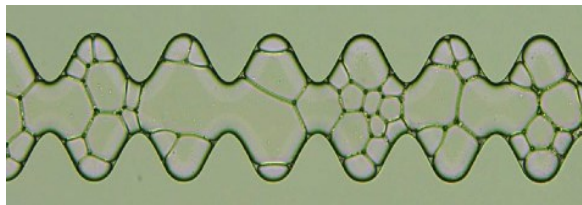
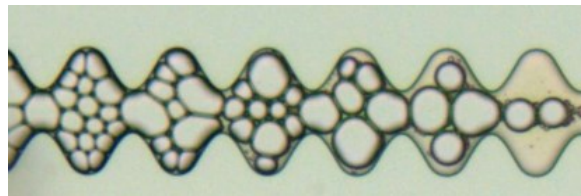
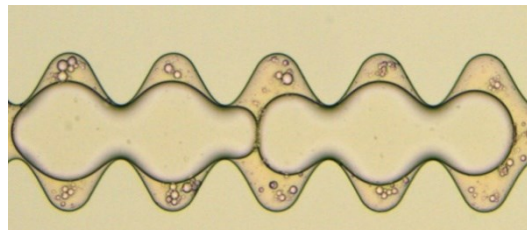


Figure 35. Evolution of flow with time.

c. $AR=4.5, \lambda=100 \mu\text{m}$

Similar to AR 3.2, AR 4.5 had a constant concave front. However, the emulsions were not flowing prior or stuck at the interface. They instead appeared as dots in the oil phase in the pores (Figure 36).

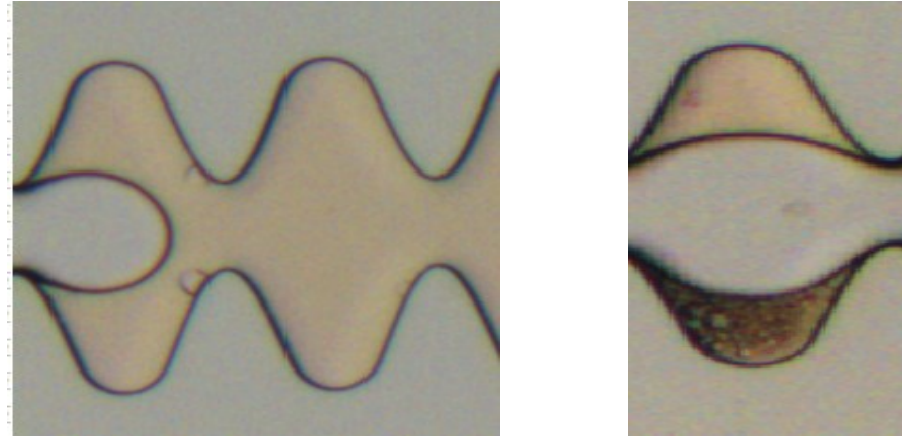


Figure 36. Initial front displacement: remained symmetrical concave with small dot like emulsions trapped in the remaining oil.

Slug flow was also present with different sizes of emulsions (Figure 37 - top). As a final state in Figure 37 - bottom, we can see bigger emulsions trapped in the pore spaces that do not coalesce into the larger droplets but rather have vivid discrete interfaces. Large clusters dominate the system. This is contrary to what is seen in AR 3.2, where with time progression, more foam-like emulsions are attached to the pore body walls (Figure 35).

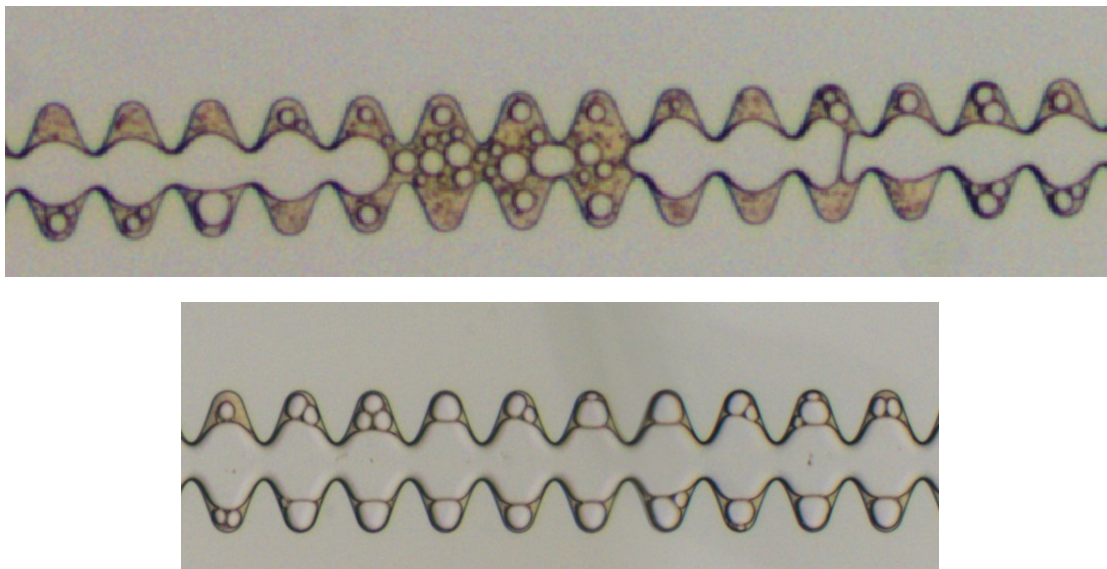


Figure 37. Evolution of flow with time.

Comparison of emulsion characteristics for flow after BT

Table 10 allows us to differentiate between the near-optimum and over-optimum conditions in terms of emulsions and flow types. In both, we can see foam-like emulsions. The term "foam-like" is taken from Kharrat et al., 2022 [16] because even though this is a water-oil mixture, it closely resembles foam flooding conditions. The foam in this case is made up of the water/surfactant phase enclosed in oil based lamellae. This happens because of the oil-wet system where the lamella attaches to the pore surfaces.

The near-optimum case shows a higher degree of solubilization. The lamellae are easily formed but are unstable. The foam-like emulsion also flow with the aqueous solution. With time, the lamellae break, and a single fluid phase flows through the system, as seen with AR 1.6. with AR 3.2, even though some foam-like emulsions remain in the pore bodies at that time, we expect with enough injection time, complete solubilization will occur. In AR 4.5, no foam-like emulsions appeared, and the flow changed directly from slug to complete solubilization.

With the over-optimum case, we have more discrete interfaces between the bubbles. The flow changed from slug to foam-like. The visualization of macroemulsion structures and drop-traffic flow may be due to this flow transition, as seen in Kharrat et al., 2022 [16] work. With an increase of AR from 1.6 to 4.5, the amount of oil in the system increases. Therefore, the foam quality decreases. The foam quality is the ratio of the inner phase (the aqueous solution in our case) to the total fluid volume.

We also notice that with AR 3.2, in both cases, we have the most classical foam-like emulsion generation, with the latter having more discrete interfaces.

In both cases, oil displacement is done through separating interfaces (slug flow and classical drainage) and also through the thin films in the foam structures.

Table 10. Emulsion comparison between different ARs and injected fluid.

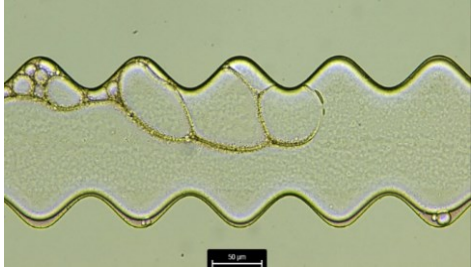
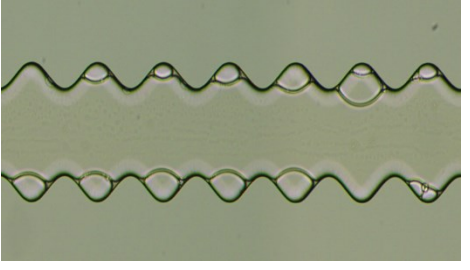
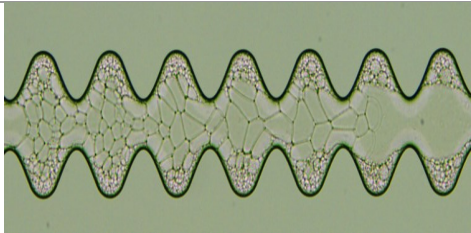
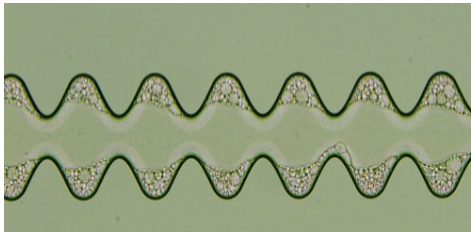
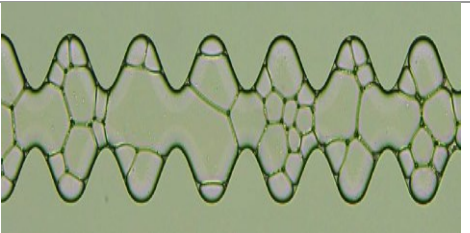
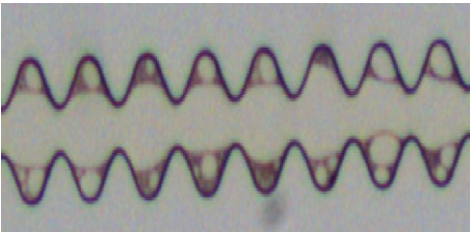

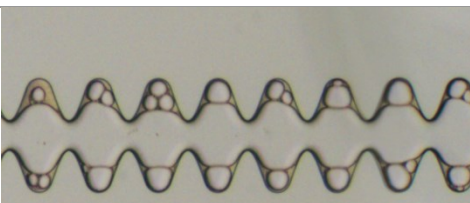
	2%	4%
AR 1.6		
AR 3.2	 	 
AR 4.5		

Table 11 combines all that was discussed in the previous sections. We can notice that for $AR=4.5$ and 3.2 , the displacement front was concave, and trapped oil was present for all types of injected fluid. However, emulsions were formed only in over-optimum conditions along the initial displacement front. As the AR decreased to 1.6 , the front shape varied with the injected fluid. With DI injection, it was concave, then changed to alternating concave and convex with the near-optimum case, then changed to concave to diagonal with the over-optimum case.

We can assume that as the AR decreases, the front shape is more prone to alteration when changing the injected fluid, and displacement is more efficient with surfactant injection (no trapped oil). Furthermore, as previously expected, no emulsions were seen with DI injection. For surfactant flooding, emulsions were always spotted in the over-optimum injection except for the $AR=1.6$, while the near-optimum case only showed minor emulsions for $AR=1.6$, which

again shows that a low AR behaves differently than higher ARs when injecting surfactant solutions in terms of emulsions formation.

Table 11. Comparison between different ARs and injected fluid.

	DI	2%	4%
	AR = 1.6		
Front shape	Concave	Alternating concave and convex	Concave to diagonal
Trapped oil	Yes	No	No
Emulsions	No	Yes	No
	AR = 3.2		
Front shape	Concave	Concave	Concave
Trapped oil	Yes	Yes	Yes
Emulsions	No	No	Yes
	AR = 4.5		
Front shape	Concave	Concave	Concave
Trapped oil	Yes	Yes	Yes
Emulsions	No	No	Yes

5.2.2 Remaining Oil saturation

For DI injection, final RF can be used because after breakthrough, no change was observed (Figure 23). Thus, the amount of oil left in the system no longer changes, and we can calculate a constant RF.

On the other hand, we cannot calculate an accurate final RF for surfactant injection because the oil trapped in the system changes with time (seen in Figure 38). Generally, most of the trapped oil was mobilized. In order to compare different conditions in terms of trapped oil, average ROS is used during first contact displacement.

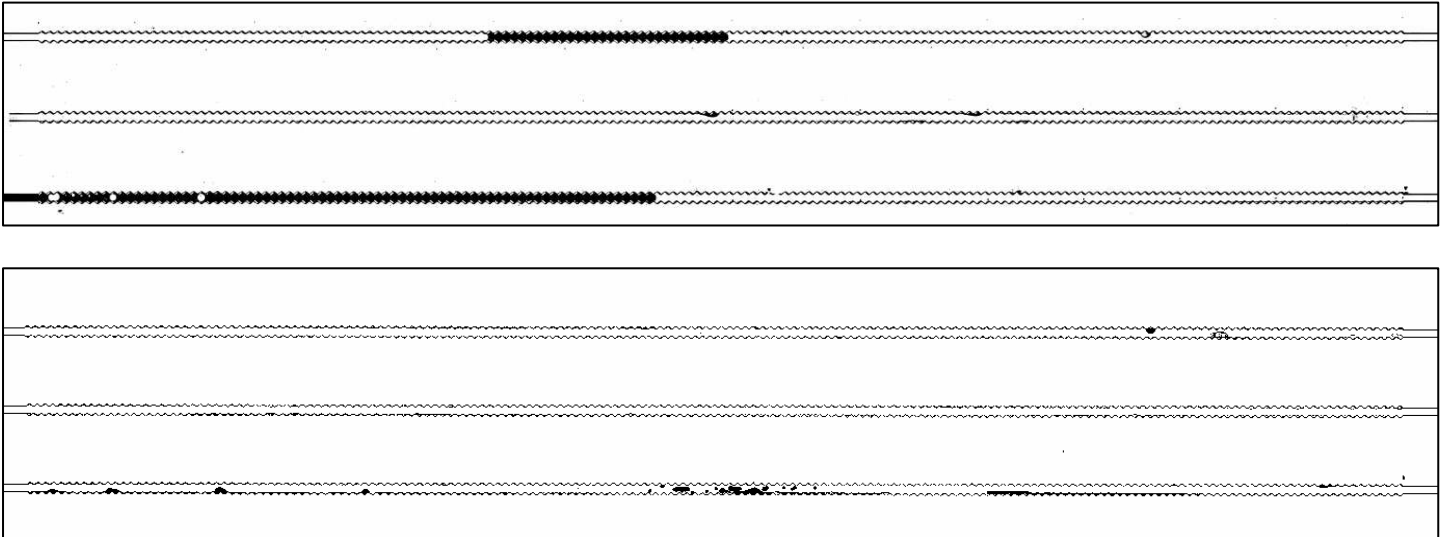


Figure 38. AR 1.6, over-optimum case. Trapped oil reduces over time. Interval time: 15 minutes. Figure in binary from ImageJ.

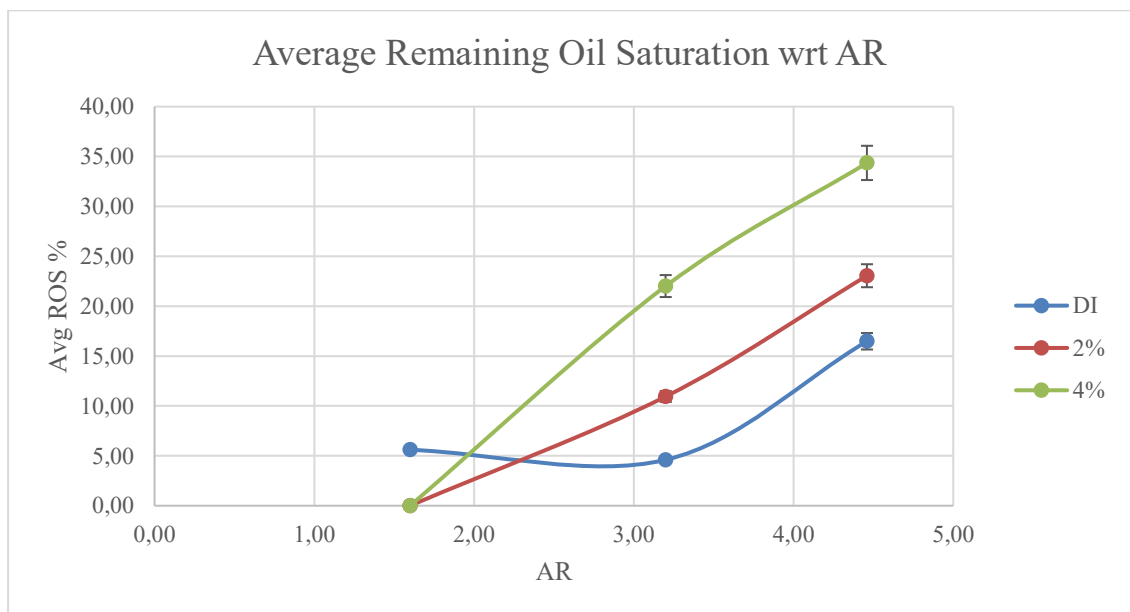


Figure 39. Average remaining oil saturation after first contact displacement with different ARs and injected fluid.

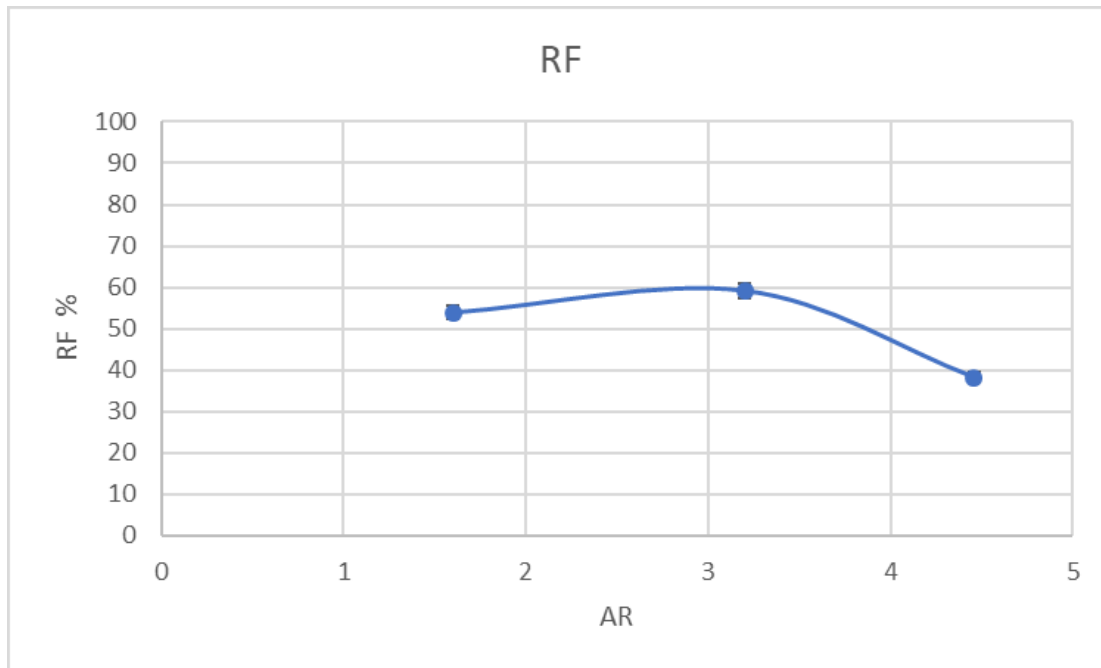


Figure 40. DI injection RF with different ARs.

Figure 39 allows us to conclude that the average remaining oil saturation increases with AR and salinity of injected surfactant solution. Since we are discussing flow in only one channel, we can conclude that as AR and/or surfactant solution's salinity increases, displacement efficiency decreases. As for DI injection, ARs 1.6 and 3.2 had similarly close values of initial average ROS, which was less than AR 4.5. This same trend was also noticed for final RF (Figure 40). AR 1.6 and 3.2 have lower ROS meaning a good displacement efficiency. For AR 4.5, the displacement and sweep efficiencies are low because two channels were bypassed.

5.2.3 Velocities

The front velocities are affected by bypassing, so their trend may increase or decrease as time progresses, but generally fall into the same or approximate ranges.

Table 12 Front velocities wrt initial in $\mu\text{m/s}$.

	AR=1.6	AR=3.2	AR=4.5
DI	1-7	9-30	20-60
2%	5-8	18-31	55-80
4%	4-8	30-50	-

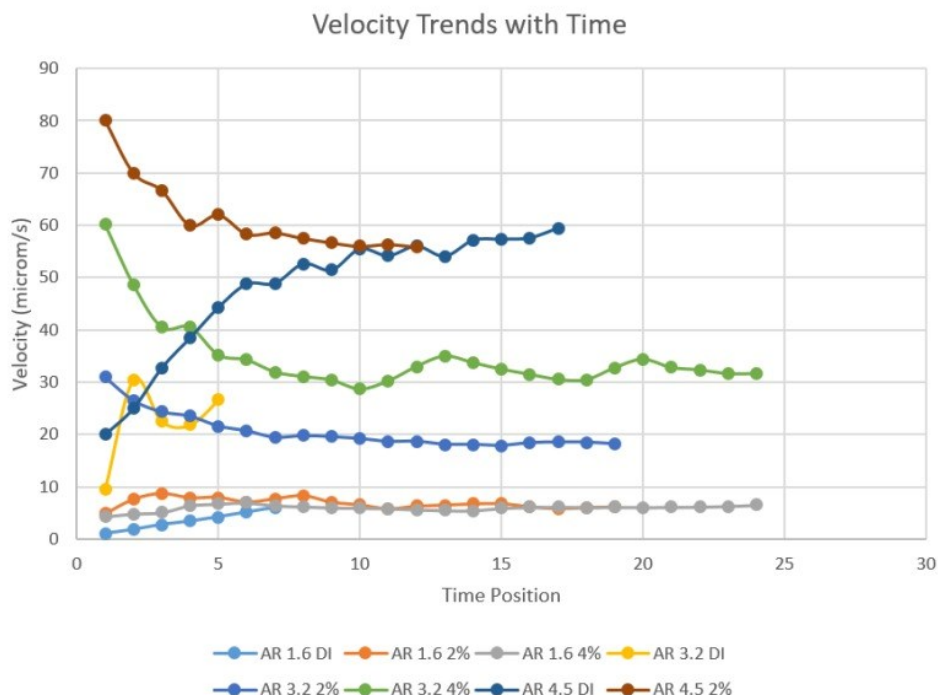


Figure 41. Evolution of in situ front velocities with time for different ARs and injected fluids.

The calculation of average velocity ranges, seen in Table 12 and Figure 41 allows us to correlate the average ROS with the AR. Some clear trends arise. For the same injected fluid, as AR increases, velocity increases, and so does the average ROS. This could be due to less contact time between the oil and surfactant solution in higher velocities. A much higher range of velocities was observed in DI injection for AR 4.5 compared to the other two ARs. This may be related to bypassing channels.

This trend is also visible when keeping a constant AR but changing the injected fluid. With AR 3.2, the ranges of a front velocities increase from DI injection to near optimum and to over optimum case, resulting in an increased average ROS, respectively.

For AR 1.6, even though all injected fluids had the same average front velocity, only surfactant injection resulted in no initial trapped oil. Moreover, AR 1.6 exhibited the slowest speeds compared to all other ARs. This may be the reason why the front shape was more prone to alteration. As the general ranges of front velocities increase, the front can stabilize into concave shape.

In order to see how velocities change throughout each channel, velocity with respect to the previous point in calculated. This allows us to see how velocities are changing depending on their location in the pore and pore radius. We will be taking the AR 1.6 case since this is where

the front and emulsion presence were most prone to alteration. For AR 1.6, the pore, throat, and slide (halfway) radius are 155, 96.7, and 125.85 μm , respectively.

DI Injection

Front shape: Concave, Trapped oil: Yes (Average Sor: 5.606%), Emulsions: No, time interval: 0.248 sec

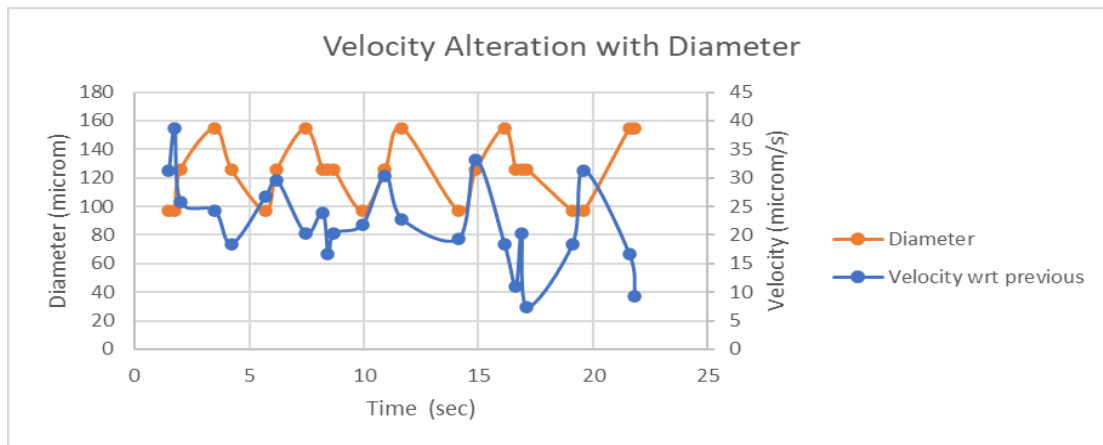


Figure 42. Velocities wrt previous vs time and pore diameter (radius).

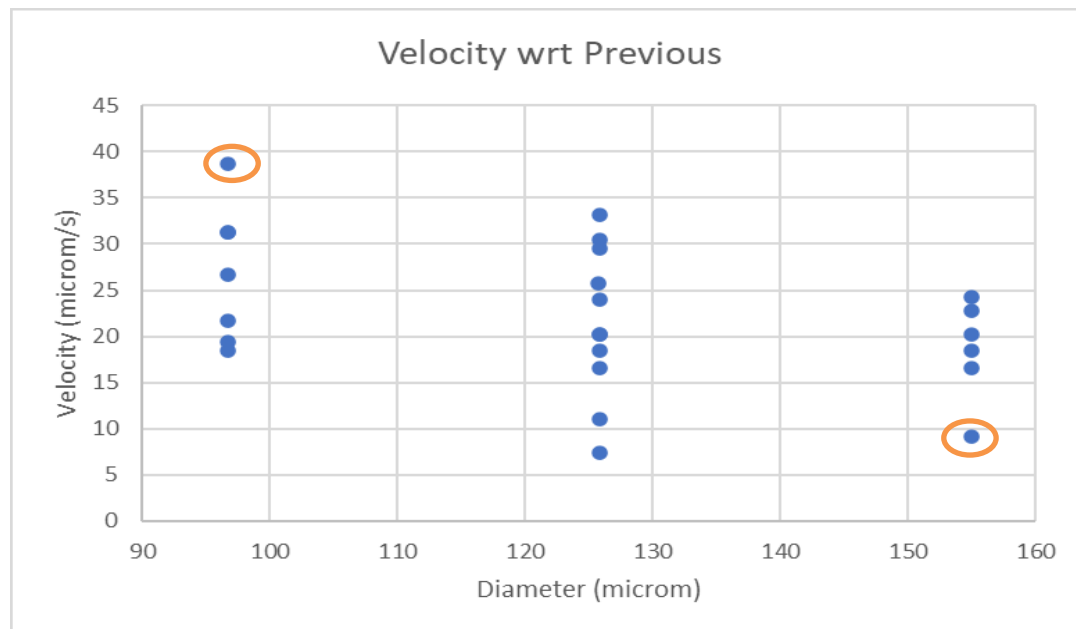


Figure 43. Velocity wrt previous vs. pore diameters (radii): 155, 96.7, and 125.85.

In Figure 42, the velocity wrt previous alternates from 5 to 40 $\mu\text{m}/\text{sec}$. The velocity usually peaks as the diameter increases, meaning the front moves faster from the pore throat to the pore body. On the contrary, the front moves the slowest, moving from high diameter to low. This is shown in Figure 43, where we can see that with the middle diameter of 125 μm , we have a wider

velocity range, with the highest values for the fluid movement between pore throat and body and the lowest values vice versa. The marked values for the diameter of 97 (throat) and 155 (body) are likely to be outliers because they occur at the beginning and end of the experiment.

Near-optimum case

Front shape: Alternating concave and convex, Trapped oil: No, Emulsions: Yes, time interval: 0.248 sec

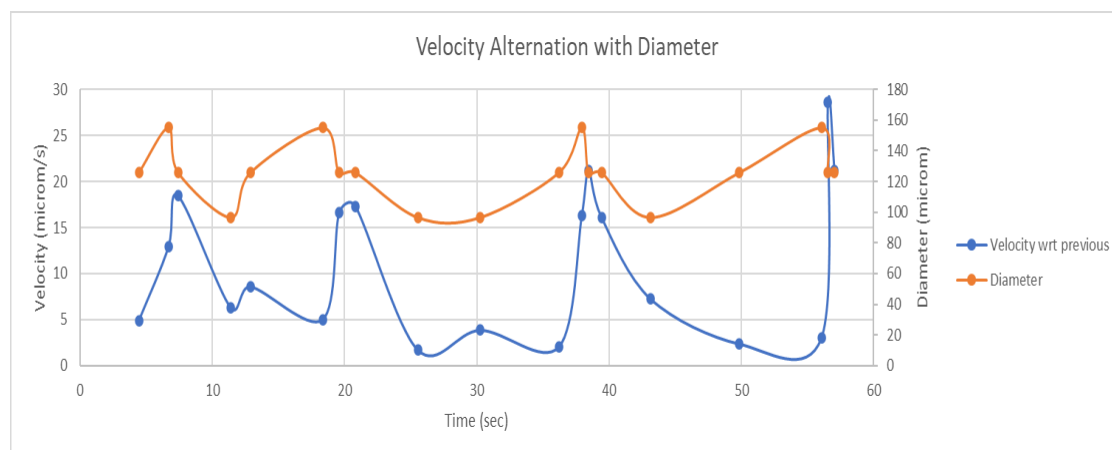


Figure 44. Velocities wrt previous vs time and pore diameter (radius).

As seen in Figure 45, while moving from the narrow part (pore throat) to the wide part (pore body), the front has a symmetrical concave shape with the tip into the oil phase. The concavity degree becomes more significant as the front approaches the pore body while still keeping its symmetrical shape. Directly after the front reaches the tip of the pore body, the concave shape changes and becomes vertical with no concavity. Next, the front shape changes to convex (with the tip into the surfactant phase) until it reaches the beginning of the throat. At the throat, the cycle starts again with a concave front shape. In all of this cycle, the front keeps a concave shape much longer than a convex one.

As for the front speed, in the pore throats, having a concave shape, it takes longer to move and seems to push the oil with greater difficulty. Displacement here is slow. However, as seen in Figure 44, the front passes through the pore body more quickly and peaks its speed in the slide from the body to the throat. The velocity wrt previous has a broader range from 1 to 28 $\mu\text{m}/\text{sec}$.

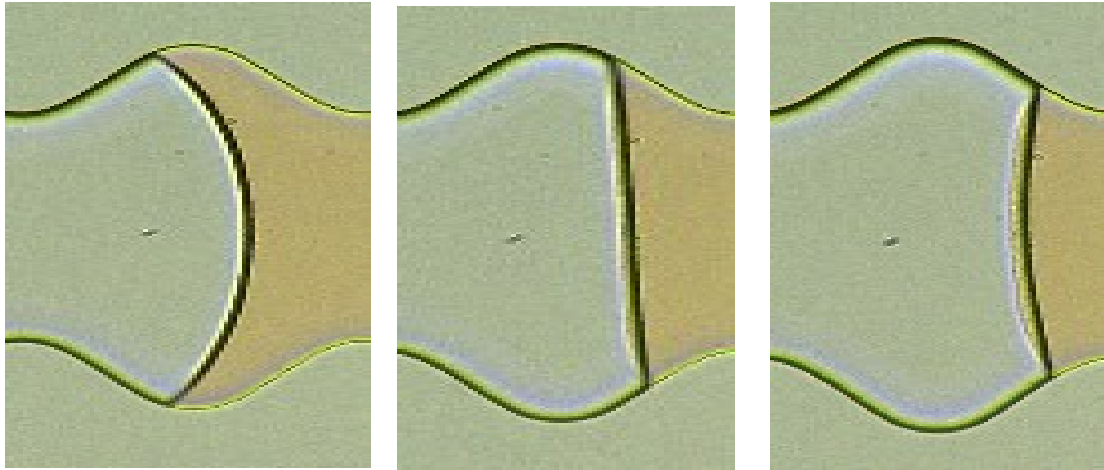


Figure 45. Alteration of front shape from concave to convex (left to right).

Over-optimum case

Front shape: Concave to diagonal, Trapped oil: No, Emulsions: No, time interval: 0.248 sec

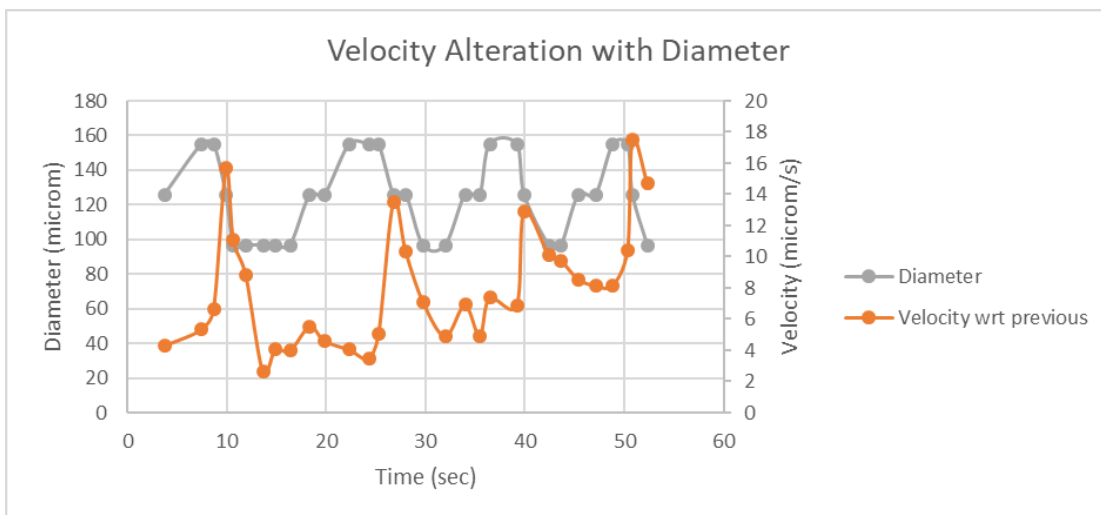


Figure 46. Velocities wrt previous vs time and pore diameter (radius).

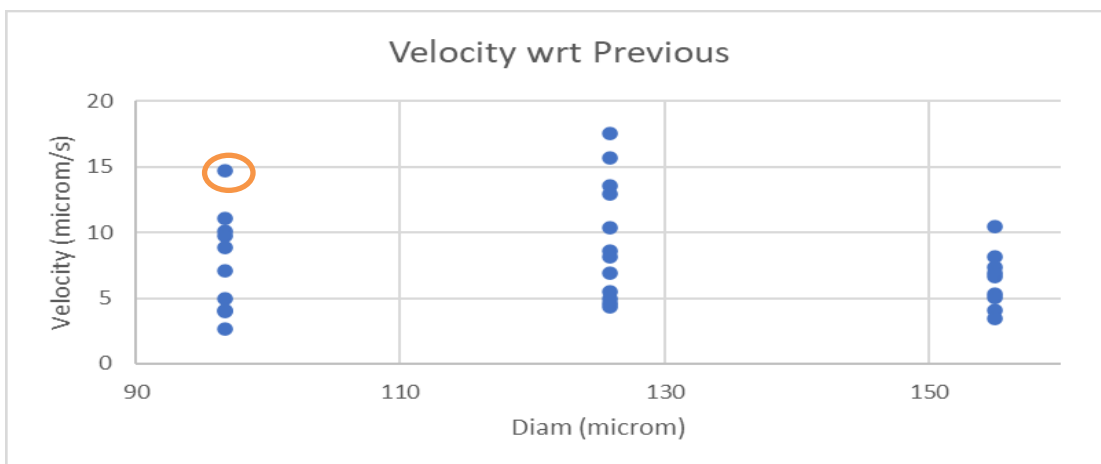


Figure 47. Velocity wrt previous vs pore diameters (radii): 155, 96.7, and 125.85.

As seen in Figure 46 and Figure 47, the front shape changes from concave symmetrical in the throats to diagonal in the pore bodies. Contrary to the previous case, velocity wrt previous has a smaller and lower range from 2 to 18 $\mu\text{m}/\text{sec}$. The highest velocity values were experienced when the front was in the slide, moving from pore body to throat. The velocities in the pore bodies, pore throats, and slide from throat to body all had the same ranges of 3 to 100 $\mu\text{m}/\text{sec}$, with the point in orange being an outlier because it is at the end of the experiment.

Table 13. Description of all flow parameters for AR 1.6 with DI, 2%, and 4% injection.

Front shape	Trapped oil	Emulsions	AR	Injected	Fast movement	Slow movement	Velocity wrt Previous Range
Concave	Yes	No	1.6	DI	Slide from throat to body	Slide from body to throat	5-40
Alternating Concave and Convex	No	Yes	1.6	2%	Slide from body to throat (where we have this alternating movement).	throat	1-28
Concave to diagonal	No	No	1.6	4%	Slide from body to throat	Everything else	2-18

Here again we can notice from Table 13. Description of all flow parameters for AR 1.6 with DI, 2%, and 4% injection. that the front speed, whether calculated point by point or taken as an average, affects the front shape and displacement efficiency. Fast movement (DI injection) had a constant concave shape (viscous-dominated flow) and more trapped oil.

5.3 Generic fluids — Different λ , AR =8, Low Injection rate (0.0008 ml/h)

Table 14. Comparison between different λ s and injected fluid.

	DI	2%	4%
	$\lambda = 500 \mu\text{m}$		
Front shape	Concave	Concave	Concave
Trapped oil	No	No	Yes (<4%)
Emulsions	No	No	Yes
Figure	Figure 48 top	Figure 48 middle	Figure 48 bottom
	$\lambda = 2500 \mu\text{m}$		
Front shape	Concave	Concave	Concave
Trapped oil	No	No	Yes (<2%)
Emulsions	No	No	Yes
Figure	Figure 49 top	Figure 49 middle	Figure 49 bottom

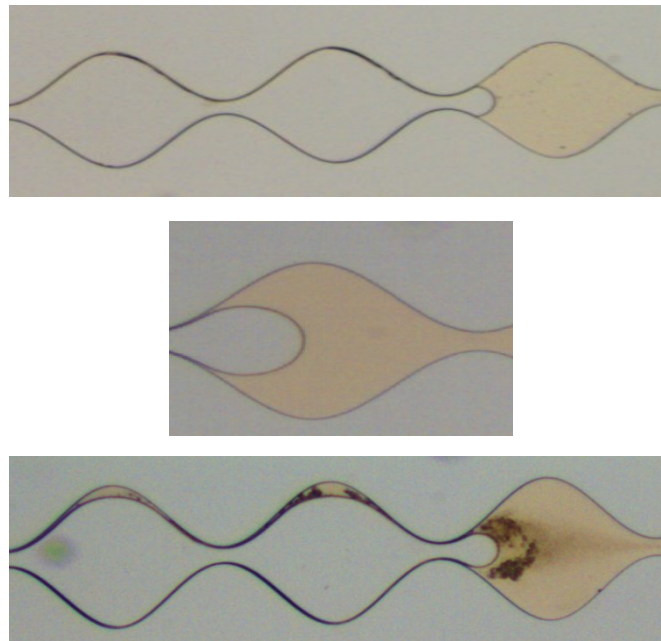


Figure 48. First contact displacement for $\lambda=500 \mu\text{m}$. Top: DI injection with concave front and no trapped oil. Middle: near-optimum condition with concave front. Bottom: over-optimum condition with concave front and emulsions in trapped oil and prior to the front

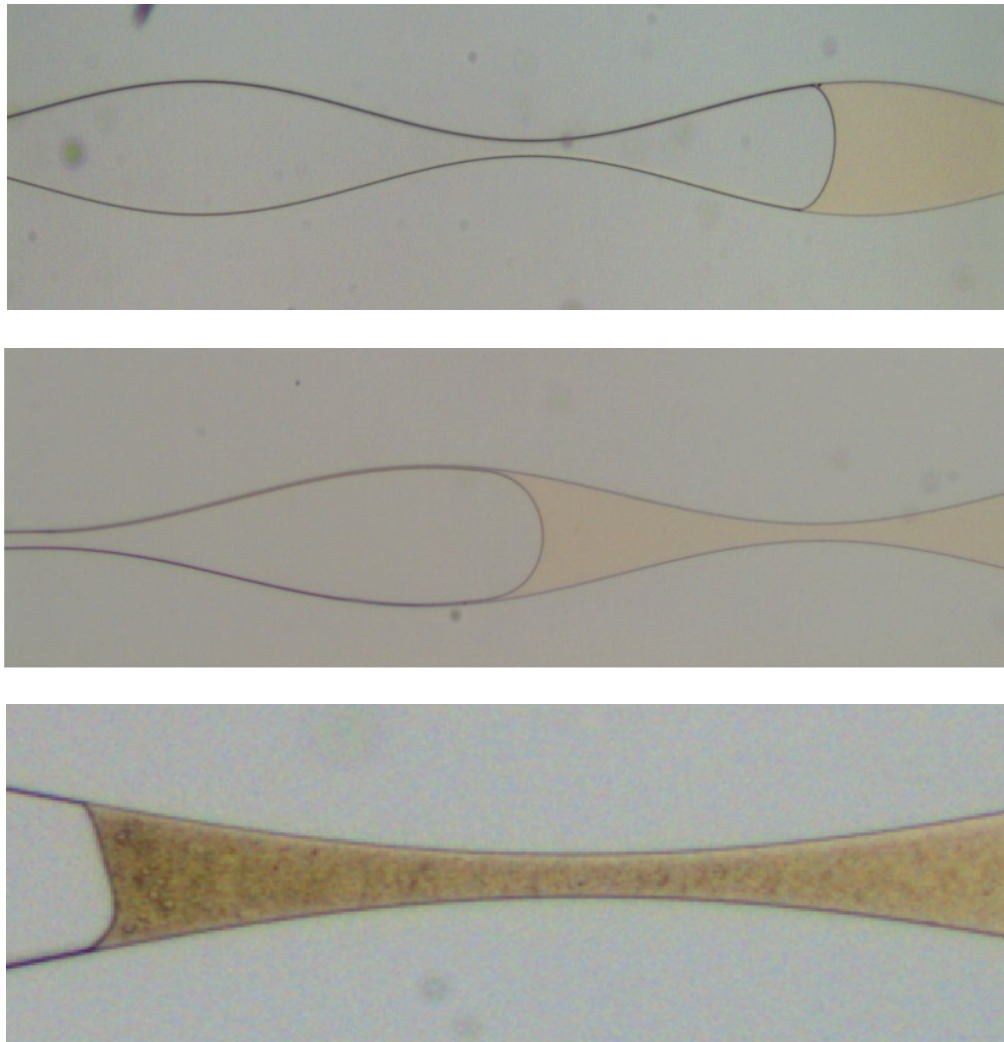


Figure 49. First contact displacement for $\lambda=2500 \mu\text{m}$. Top: DI injection with concave front and no trapped oil. Middle: near-optimum condition with concave front and no trapped oil. Bottom over-optimum condition with concave front and prior to the front

able 14 shows that for the same AR and injected fluid, increasing the distance between the pores from 500 to 2500 μm does not affect the qualitative results. Only changing the type of fluid injected leads to different visualizations and emulsion production. As for the average ROS during first contact displacement, all values were very low ($<4\%$), which is in the error margin range.

In the previous section “Remaining Oil saturation”, the avg ROS increased as the AR increased from 1.6 to 4.5. However, this AR of 8, which is much greater than all previously used ARs, resulted in a much less average ROS. This may be because for these ARs of 8, the distances between the pores are larger, and the pore body sizes are also 2 to 3 times larger. As for emulsion visualization, only with the over optimum conditions were the emulsions spotted (tight, dot-like, and flowing with the decan phase), which agrees with the results in section “First contact displacement and emulsion characterization”. Thus, we can assume that first

contact emulsion formation is more influenced by the type of injected fluid rather than by AR and distance between pores.

As for emulsions seen later in all channels with surfactant injection, different types of emulsions were arising, even in different channels. For instance, in both $\lambda=500$ with 4% injection, we can see complete solubilization in one channel and foam-like emulsions in the other (Figure 50 - top). In $\lambda=2500$ also in the over-optimum case, one channel had more loose solubilized emulsions flowing, while the other had more discrete interfaces (Figure 50 - middle). However, independent of the injection time or AR, the final result was complete solubilization (Figure 50 - bottom).

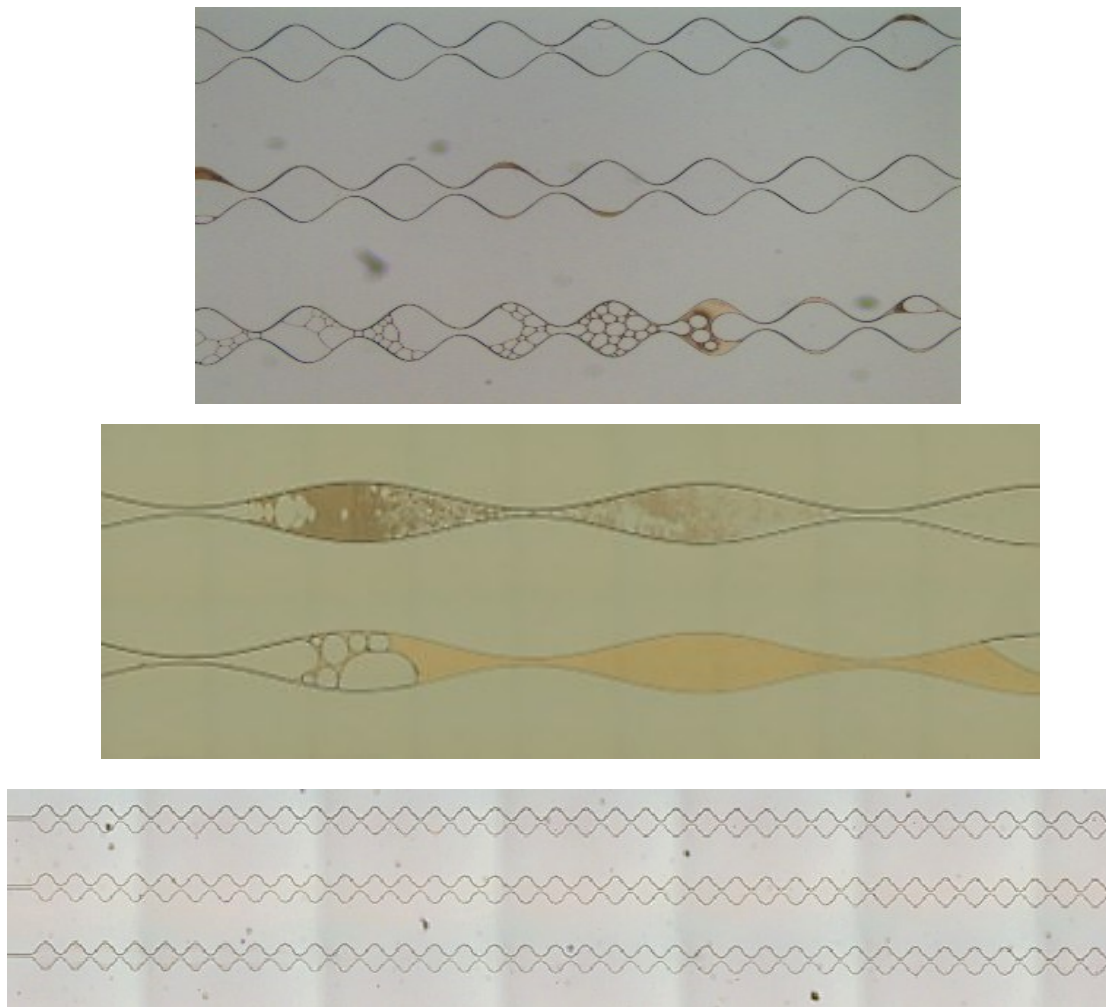


Figure 50. Different emulsion forms in different channels. Top: $\lambda=500$, over-optimum case Middle: $\lambda=500$, near-optimum case. Bottom: complete solubilization, $\lambda=500$ with near-optimum case

5.4 Generic fluids — Different Injection rates, ARs =1.6 & 3.2, same λ

Surfactant Injection

Table 15. Comparison between different injection rates, ARs, and injected fluid.

	2%		4%	
	0.005 ml/h	0.0008 ml/h	0.005 ml/h	0.0008 ml/h
	AR=1.6		AR=1.6	
Front shape	Concave	Alternating concave and convex	Concave	Concave to diagonal
Trapped oil	Yes	No	Yes	No
Emulsions	Yes	Yes	Yes	No
Figure	Figure 51 (1)		Figure 51 (2)	
	AR=3.2		AR=3.2	
Front shape	Concave	Concave	Concave	Concave
Trapped oil	Yes	Yes	Yes	Yes
Emulsions	No	No	Yes	yes
Figure	Figure 51 (3)		Figure 51 (4)	

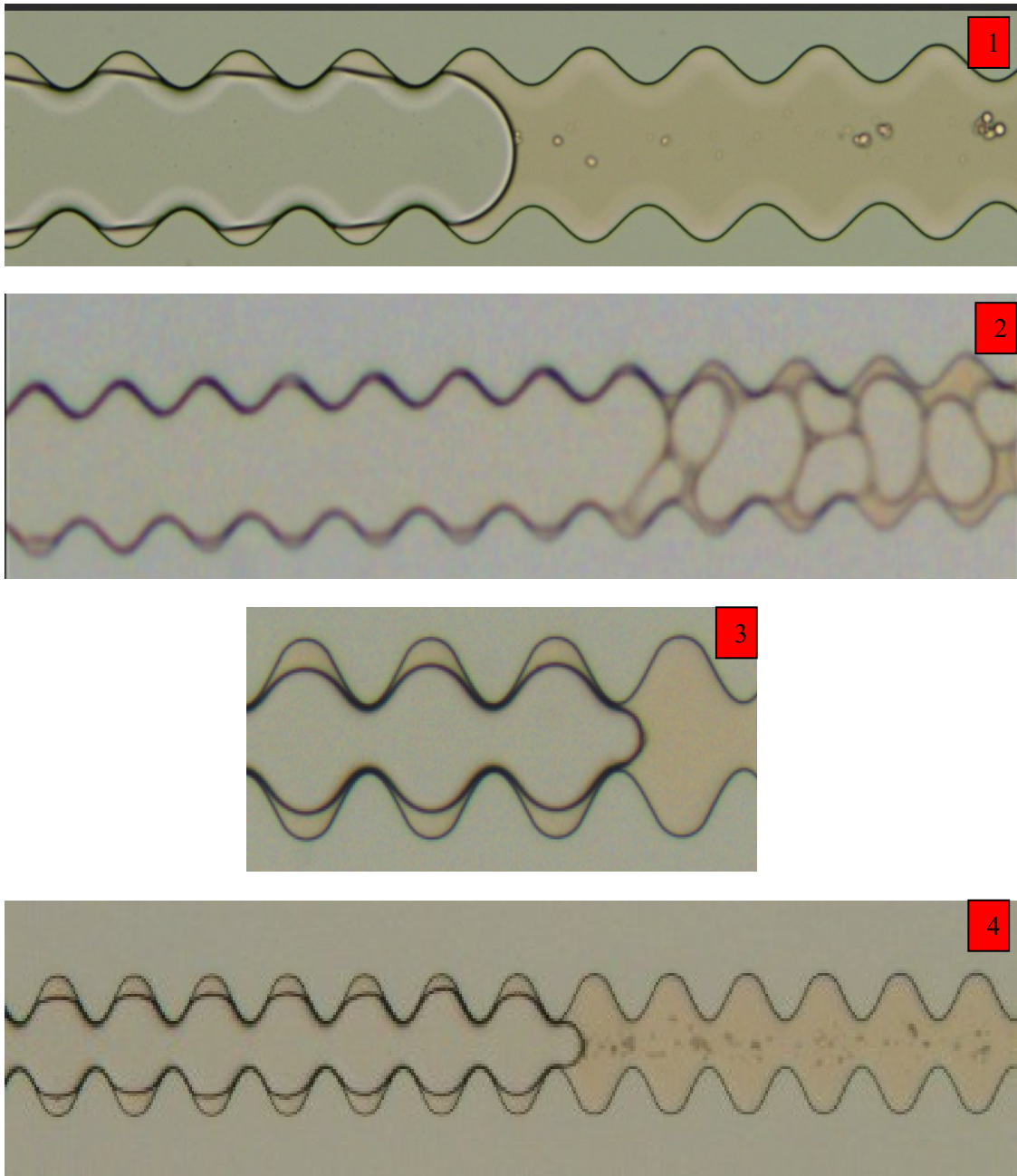


Figure 51. Initial displacement flow for high injection rate (0.005 ml/h) 1 (highest): $AR=1.6$, near-optimum case . 2: $AR=1.6$ over-optimum case. 3: $AR=3.2$ near-optimum case. 4 (lowest): $AR=3.2$, over-optimum case

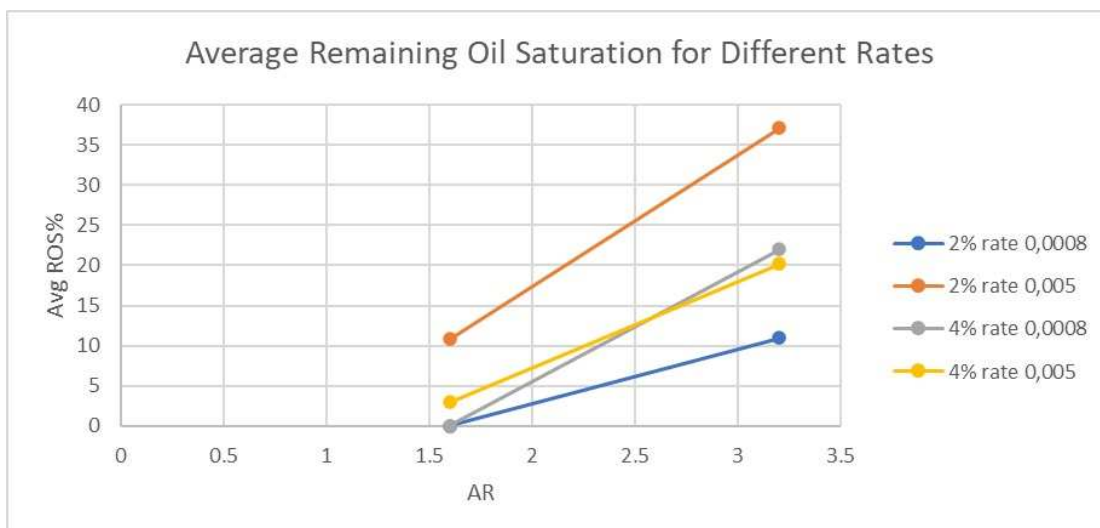


Figure 52. Comparison of average remaining oil saturation for first contact displacement with different rates.

As seen in Table 15, increasing the injection rate did not affect the higher AR of 3.2, irrespective of the injected fluid. On the other hand, the injection rate had a more significant impact on the lower AR of 1.6 where it led to trapped oil, visualization of emulsions, and stabilization of a concave displacement front for both near and over-optimum. We can therefore assume that injection rate plays a greater role for lower ARs. The assumption here is that when the injection rate increased, the front rate increased as well, meaning that flow moved into viscous dominated instead of capillary dominated. Hence, we have the stabilization of the front.

Regarding average ROS and Figure 52, for the near optimum case, there was a noticeable increase in oil trapped for both low and high ARs, with the latter AR's increase in ROS being more drastic. On the other hand, the over optimum case showed a minor change in average ROS for both AR 1.6 and 3.2. Both rates followed the same trend on the increase in avg ROS, which is increased with AR. However, contrary to what is seen for rate 0.0008 ml/h, at rate 0.005 ml/l the near-optimum case resulted in a much higher avg ROS than the over-optimum case, more drastically at AR 3.2. Thus, we can assume that near-optimum surfactant injection is highly sensitive to rate.

For high rates, less bypass was happening, and the surfactant solution entered three channels simultaneously. The velocities calculated reflect the front velocity of the channel that first contacted the surfactant solution. With the low rates, bypass was also happening, but the front velocity of the channel that first contacted the surfactant solution remained the fastest. This is not the case for high rates, where channels were competing with each other (Figure 53).

Moreover, more complex phenomena were happening where first contact displacement was actually slug flow that preceded the surfactant mixture front, which is an entirely new visualization (Figure 54).

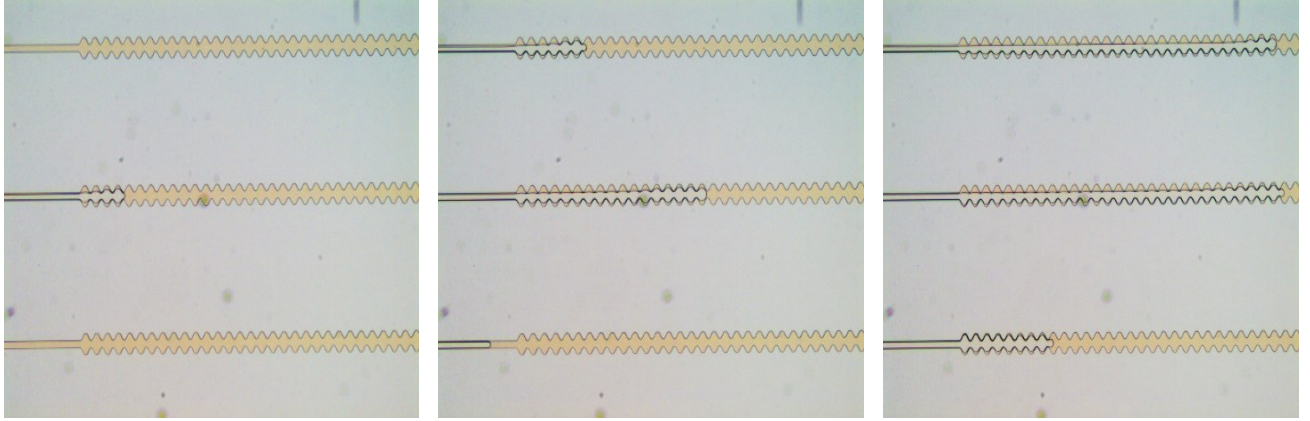


Figure 53. $AR=3.2$ with 2% surfactant injection. Different channels with different front velocities.

The time interval between the pictures is 12.25 seconds.

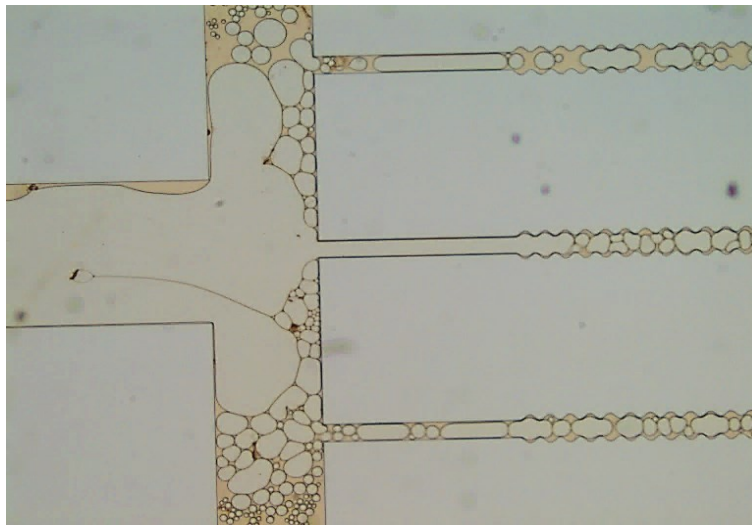


Figure 54. Slug flow preceding surfactant front.

Emulsions later on had a high degree of solubility as well (Figure 55).

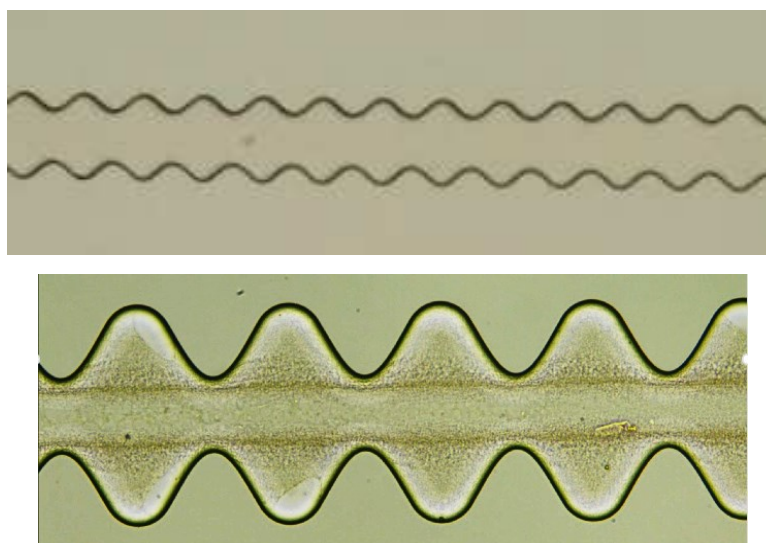


Figure 55. Emulsions with high degree of solubility. Top: $AR=1.6$ with 2% surfactant injection.

Bottom: $AR=3.2$ with 4% surfactant injection

5.5 Crude Oil — different AR, $\lambda=100 \mu\text{m}$, and low injection rate (0.0008 ml/h)

During alkaline injection (3000 and 7500 ppm Na_2CO_3), a new phenomenon arises. A mix of crude oil and alkaline bubbles appear behind the alkaline front, similar to footprints.

Table 16. Comparison between different ARs and injected fluid for oil 16.

	DI	3000 ppm	7500 ppm
	AR = 1.6		
Front shape	Concave to diagonal	Concave to convex	Concave
Trapped oil	Yes	Yes	Yes
Notes	No emulsions	Emulsions seen	Footprints seen
Figure	Figure 56 top	Figure 56 middle	Figure 56 bottom
	AR= 3.2		
Front shape	Concave	Concave	Concave
Trapped oil	Yes	Yes	Yes
Notes	No emulsions	Emulsions seen – footprints seen	Footprints seen
Figure	Figure 57 top	Figure 57 middle	Figure 57 bottom

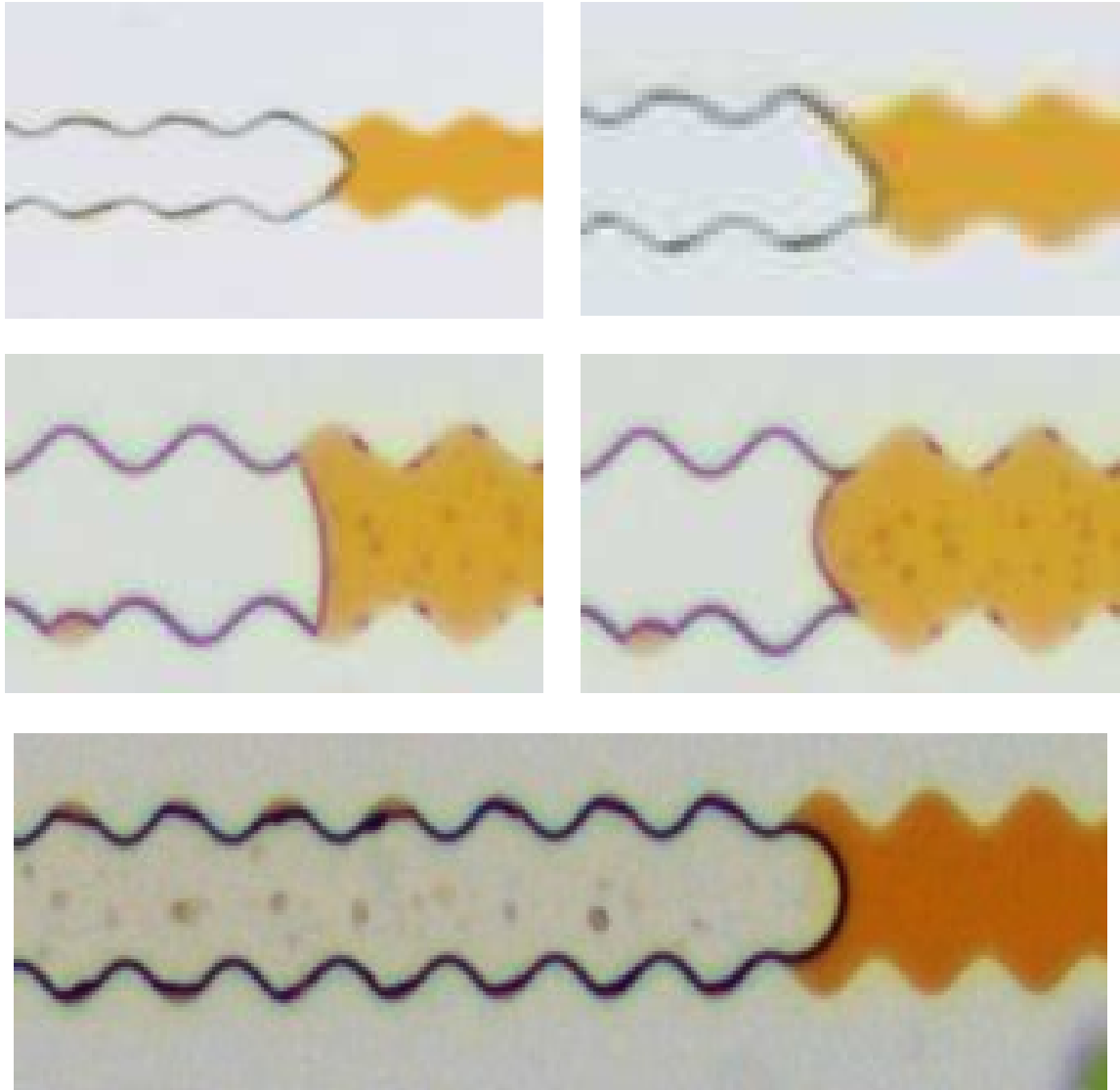


Figure 56. First contact displacement for AR 1.6. Top row: DI injection with concave to diagonal front. Middle row: 3000 ppm Na_2CO_3 injection with alternating concave and convex front with dot-like emulsions. Bottom row: 7500 ppm Na_2CO_3 injection with concave front and "footprints"

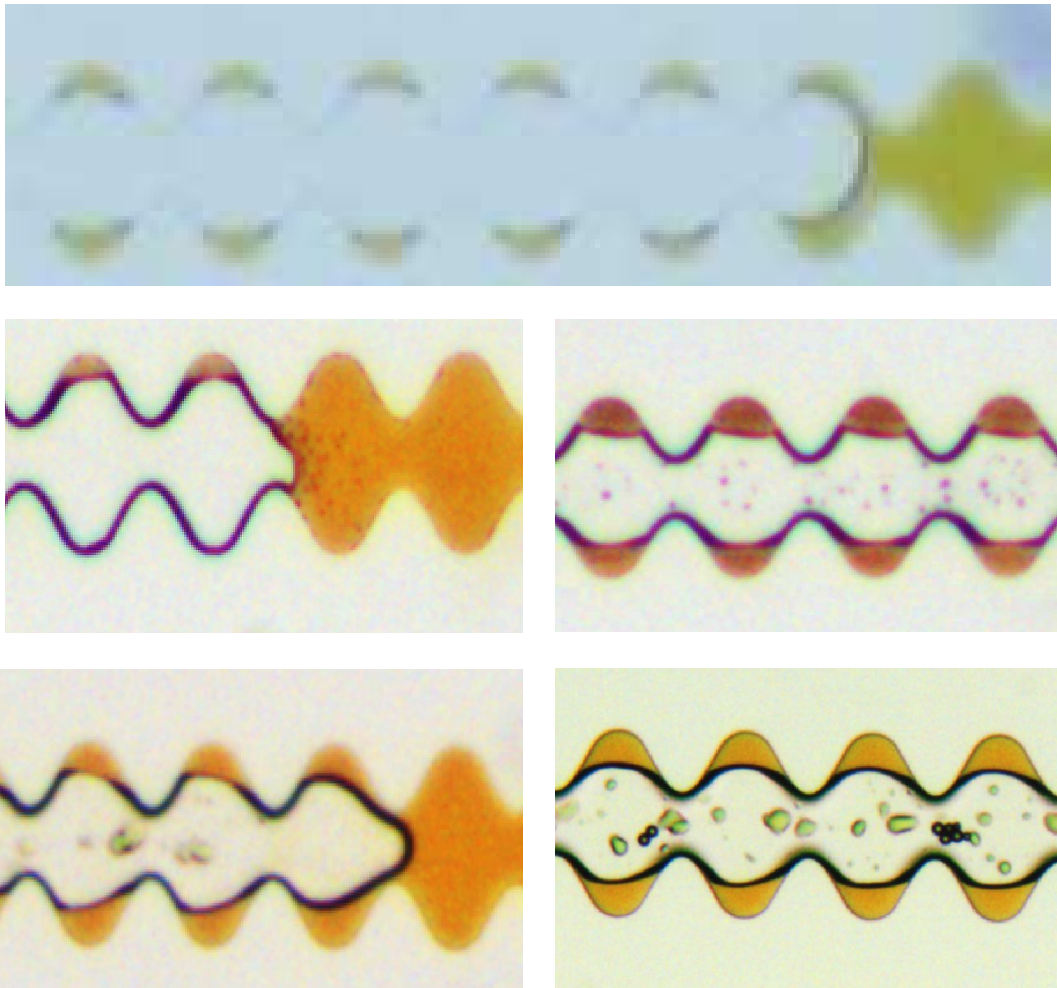


Figure 57. First contact displacement for AR 1.6. Top row: DI injection with concave front. Middle row: 3000 ppm Na_2CO_3 injection with concave front with dot like emulsions and "footprints". Bottom row: 7500 ppm Na_2CO_3 injection with concave front and "footprints"

According to Table 16, it is clear that trapped oil is always present irrespective of injected fluids. One assumed reason is that this oil has a higher viscosity and more components than decane, increasing its complexity. Hence, emulsions may get more viscous. This also may be why "footprints" are formed. These footprints stuck in place during these experiments, as seen in Figure 58. These footprints may be stuck oil (or oil and alkaline mixture) to the microchip glass. Emulsions formed later on are also very difficult to characterize since they include oil-in-water-in-oil emulsions and vice versa (Figure 59).

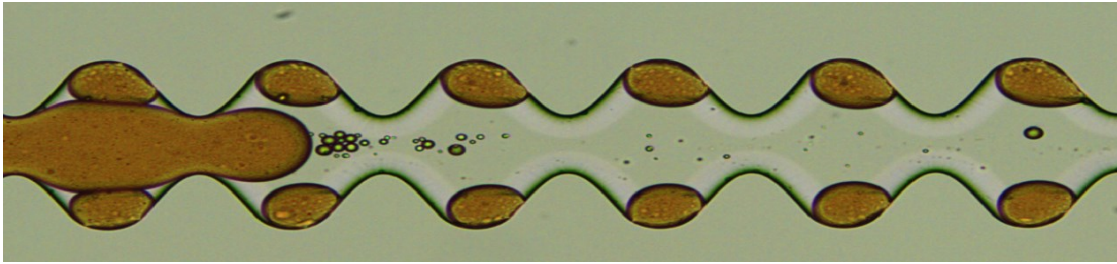


Figure 58. AR 3.2 3000ppm injection, After BT still see footprints

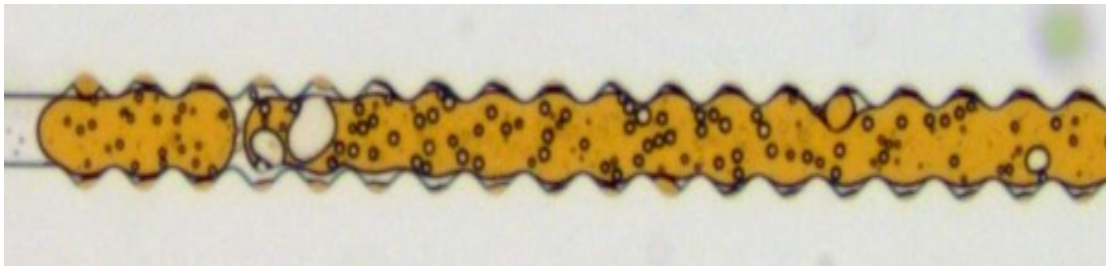
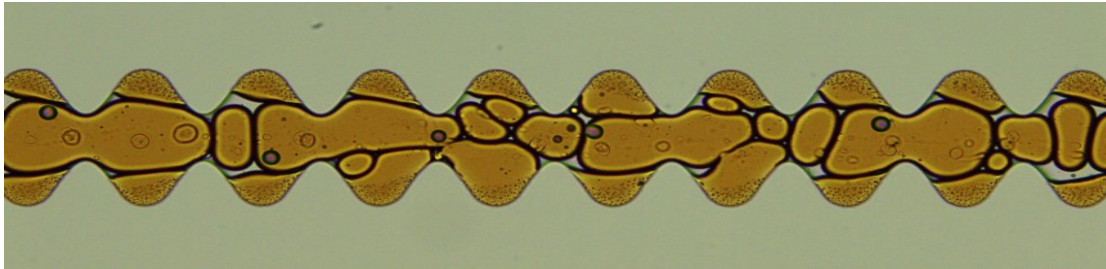


Figure 59. Complex structure. Top: AR 3.2, 7500ppm Na_2CO_3 complex oil slug flow.

Bottom: AR 1.6 7500 ppm Na_2CO_3 complex emulsions.

Similar to our previous results with generic fluid, front alteration happens in AR 1.6. This supports our previously assumed conclusion that low ARs affect the front shape. DI injection also does not produce visible emulsions when injected into heavier oil. In both ARs, the under-optimum case (3000 ppm Na_2CO_3) generated visible emulsions in the oil phase, and the optimum case (7500 ppm Na_2CO_3) produced footprints. Because we have different emulsion types, it makes comparing them more complex and not in the frame of this thesis. This needs further investigation.

When discussing trapped oil, the "footprints" are not taken into consideration. The average ROS only related to the oil trapped in the pore cavities, as seen in Figure 60.



Figure 60. Trapped oil with AR 1.6 DI injection.

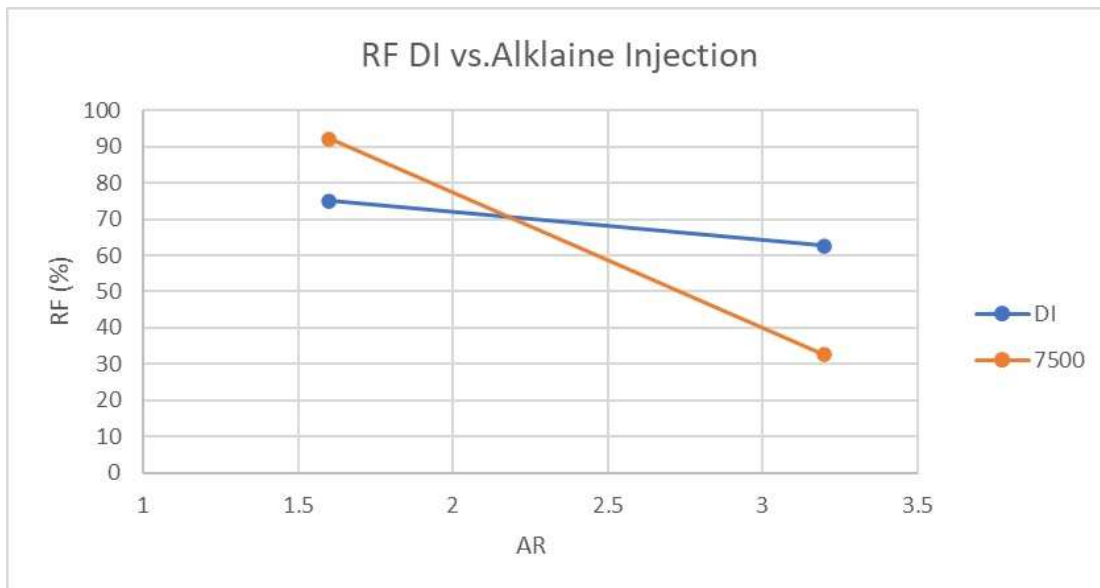
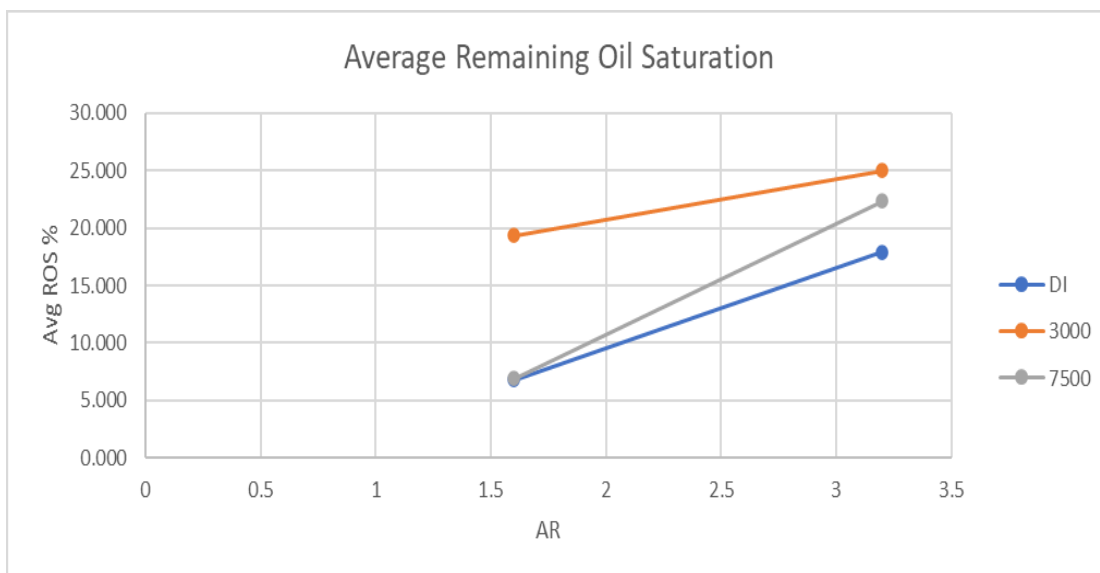


Figure 61. Remaining oil saturation with different ARs and injected fluid. Top: average ROS during first contact displacement. Bottom: final RF.

As seen in Figure 61, the under-optimum case has the most initial trapped oil. As the AR increases, so does the average ROS during initial displacement for all cases. However, this increase is most drastic for the optimum case. The optimum case is also highly affected by AR in the final RF. This leads us to assume that:

- as AR increases, both initial and final remaining oil increase
- AR value has a more significant impact on RF when injecting alkaline than when injecting DI

5.6 Summary

Table 17 summarizes all the generic-fluids experiments done in this thesis, highlighting their front shape, presence of trapped oil and emulsions, geometrical design, fluid characteristics, and flow properties.

Table 17. Summary of all experiments in terms of flow characteristics.

Front shape	Trapped oil	Emulsions	AR	λ (μm)	Injected	Injection rate (ml/h)
Concave	Yes	No	1.6	100	DI	0.0008
			3.2	100	2%	0.0008
			4.5	100	DI	0.0008
			4.5	100	2%	0.0008
			3.2	100	2%	0.005
			3.2	100	DI	0.0008
Concave	Yes	Yes	3.2	100	4%	0.0008
			4.5	100	4%	0.0008
			1.6	100	2%	0.005
			1.6	100	4%	0.005
			3.2	100	4%	0.005
			8	500	4%	0.0008
			8	2500	4%	0.0008
Concave	No	No	8	500	DI	0.0008
			8	2500	DI	0.0008
			8	500	2%	0.0008
			8	2500	2%	0.0008
Concave to diagonal	No	No	1.6	100	4%	0.0008
Alternating Concave and Convex	No	Yes	1.6	100	2%	0.0008

Chapter 6

Conclusion

6.1 Summary

In summary, characterization of emulsion and fluid displacement have been studied during first contact displacement and later times throughout the injection process. For the prior, the emphasis was on front shape and stability, remaining oil in the pores, visualization of emulsions, and in-situ front velocity. Emulsions were also studied during the displacement process to see how time affects their solubility, rigidity, and stability. Because pore geometry, fluid characteristics, and flow parameters affect emulsion sizes and their stability, these properties varied from one experiment to another. Pore geometry effects were the highlight of this study, mainly how changing the aspect ratio affects fluid displacement.

A different set of fluids were used in this thesis, such as generic fluids (decan and surfactants) and crude oil with sodium carbonate as an alkaline agent. In order to form several types of emulsion, different solutions were made to generate near-optimum and out-of-optimum conditions for both sets of fluids. In addition, different injection rates were implemented for generic fluids.

For our results, we started by calculating Reynold's number. Due to drastically low Re ranges, we assumed that any emulsions seen were not due to turbulence. For the same injected fluid, by increasing the aspect ratio, we saw an increase in remaining oil during first contact displacement. For the same aspect ratio, the average remaining oil saturation increased gradually as we moved from DI injection to the near-optimum condition to the over-optimum one. We saw similar trends when we studied the in-situ front velocities. Thus, we can correlate velocity, remaining oil saturation, and AR into one relationship: As AR increases, the velocities increase, and so does the average remaining oil saturation.

When it comes to emulsion characterization, we observed that most emulsions during first contact displacement happen in the over-optimum condition, regardless of AR alteration. With time, emulsions with different characteristics emerged with near-optimum and over-optimum conditions. Foam-like emulsions were widely noticed in the majority of the experiments. The

foam-like emulsion had a higher quality with more solubilization in the near-optimum case. On the contrary, the foam-like emulsion had low quality and more discrete interfaces in the over-optimum condition.

Changing the pore geometries in terms of distance between pores and pore body sizes had a visible effect on remaining oil during first contact displacement. The larger distances between pores (500 and 2500 μm) resulted in significantly lower trapped oil than smaller distanced (100 μm). Increasing injection rates greatly affected lower ARs, mainly during the near-optimum condition.

With the alkaline injection, trapped crude oil was always present, likely due to the higher viscosity and complexity of this oil. Much more complex phenomena were seen later, making it challenging to characterize emulsions and flow.

One thing was relatively uniform throughout all experiment results, which was the front behavior of AR 1.6. Thus, we assume that lower ARs have a higher inclination to front alteration.

6.2 Evaluation

The main thesis goal was to find out how changing the simple pore geometries will affect fluid displacement. All experiments were comprised of changing the aspect ratios or distances between pores. Thus, we could better understand the influences of pore geometries, especially during first contact displacement on front shape, emulsion formation, velocity, and remaining oil. We were able to come up with a clear relationship between pore geometries and these properties.

6.3 Future work

The topic of the effects of pore geometry on fluid displacement can not only bring fruitful insights but is also relatively new and thus has a large room for exploration. Future work and building up from this thesis may comprise of:

1. Chips design: this thesis used chips that had three channels. It would be beneficial to have chips with the same dimensions and properties (AR, λ ..) but made of only one channel.
2. Pump injection rate: A more comprehensive range of injection rates could be used to see the impacts of flow rates on different AR.

References

- [1] Abalkhail, N., Liyanage, P. J., Upamali, K. A., Pope, G. A., & Mohanty, K. K. (2020). Alkaline-surfactant-polymer formulation development for a HTHS carbonate reservoir. *Journal of Petroleum Science and Engineering*, 191, 107236. <https://doi.org/10.1016/j.petrol.2020.107236>
- [2] Akbari, S., & Nour, A. H. (2018). Emulsion types, stability mechanisms and rheology: A review. *International Journal of Innovative Research and Scientific Studies*, 1(1), 11-17. <https://doi.org/10.53894/ijirss.v1i1.4>
- [3] Azam, M. R., Tan, I. M., Ismail, L., Mushtaq, M., Nadeem, M., & Sagir, M. (2013). Static adsorption of anionic surfactant onto crushed Berea sandstone. *Journal of Petroleum Exploration and Production Technology*, 3(3), 195-201. <https://doi.org/10.1007/s13202-013-0057-y>
- [4] Borji, M., Kharrat, A., & Ott, H. (2022). Comparability of in situ crude oil emulsification in phase equilibrium and under porous-media-flow conditions. *Journal of Colloid and Interface Science*, 615, 196-205. <https://doi.org/10.1016/j.jcis.2022.01.182>
- [5] Buijse, M., Tandon, K., Jain, S., Handgraaf, J., & Fraaije, J. G. (2012). Surfactant optimization for EOR using advanced chemical computational methods. *All Days*. <https://doi.org/10.2118/154212-ms>
- [6] Donaldson, Erle C.; Alam, Waqi (2008): Wettability and Production. In Erle C. Donaldson, Waqi Alam (Eds.): Wettability. Burlington: Elsevier Science, pp. 121–172.
- [7] Garstecki, P., Gitlin, I., DiLuzio, W., Whitesides, G. M., Kumacheva, E., & Stone, H. A. (2004). Formation of monodisperse bubbles in a microfluidic flow-focusing device. *Applied Physics Letters*, 85(13), 2649-2651. <https://doi.org/10.1063/1.1796526>

-
- [8] Gbadamosi, A. O., Kiwalabye, J., Junin, R., & Augustine, A. (2018). A review of gas enhanced oil recovery schemes used in the North Sea. *Journal of Petroleum Exploration and Production Technology*, 8(4), 1373-1387. <https://doi.org/10.1007/s13202-018-0451-6>
- [9] Green, Don W.; Willhite, G. Paul (2008): Enhanced oil recovery. Richardson, Tex.: Henry L. Doherty Memorial Fund of AIME Society of Petroleum Engineers (SPE textbook series, 6).
- [10] Gyan, P. S., Xie, C., Brantson, E. T., & Atuahene, S. (2019). Computer modeling and simulation for undersaturated primary drive recovery mechanism. *Advances in Mechanical Engineering*, 11(5), 168781401984194. <https://doi.org/10.1177/1687814019841948>
- [11] Hamidi, H., Mohammadian, E., Rafati, R., Azdarpour, A., & Ing, J. (2015). The effect of ultrasonic waves on the phase behavior of a surfactant–brine–oil system. *Colloids and Surfaces A: Physicochemical and Engineering Aspects*, 482, 27-33. <https://doi.org/10.1016/j.colsurfa.2015.04.009>
- [12] Haq, B., Liu, J., Liu, K., & Al Shehri, D. (2020). The role of biodegradable surfactant in microbial enhanced oil recovery. *Journal of Petroleum Science and Engineering*, 189, 106688. <https://doi.org/10.1016/j.petrol.2019.106688>
- [13] Harutyunyan, L. R., & Harutyunyan, R. S. (2019). Effect of amino acids on Micellization and micellar parameters of anionic surfactant Alpha olefin sulfonate C14–C16 in aqueous solutions: Surface tension, Conductometric, volumetric, and fluorescence studies. *Journal of Chemical & Engineering Data*, 64(2), 640-650. <https://doi.org/10.1021/acs.jced.8b00886>
- [14] Johnson, C. (1976). Status of caustic and emulsion methods. *Journal of Petroleum Technology*, 28(01), 85-92. <https://doi.org/10.2118/5561-pa>
- [15] Karatayev, M., Movkebayeva, G., & Bimagambetova, Z. (2018). Increasing utilisation of renewable energy sources: Comparative analysis of scenarios until 2050. *Energy Security*, 37-68. https://doi.org/10.1007/978-3-030-01033-1_3
- [16] Kharrat, A., Brandstätter, B., Borji, M., Ritter, R., Arnold, P., Fritz-Popovski, G., Paris, O., & Ott, H. (2022). Development of foam-like emulsion phases in porous media flow. *Journal of Colloid and Interface Science*, 608, 1064-1073. <https://doi.org/10.1016/j.jcis.2021.10.022>
- [17] Kume, G., Gallotti, M., & Nunes, G. (2007). Review on anionic/Cationic surfactant mixtures. *Journal of Surfactants and Detergents*, 11(1), 1-11. <https://doi.org/10.1007/s11743-007-1047-1>

-
- [18] Lake, L. W. (2014). *Fundamentals of enhanced oil recovery*.
- [19] Lim, J., Wong, S., Law, M., Samyudia, Y., & Dol, S. (2015). A review on the effects of emulsions on flow behaviours and common factors affecting the stability of emulsions. *Journal of Applied Sciences*, 15(2), 167-172. <https://doi.org/10.3923/jas.2015.167.172>
- [20] Liu, Z., Li, Y., Luan, H., Gao, W., Guo, Y., & Chen, Y. (2019). Pore scale and macroscopic visual displacement of oil-in-water emulsions for enhanced oil recovery. *Chemical Engineering Science*, 197, 404-414. <https://doi.org/10.1016/j.ces.2019.01.001>
- [21] Ma, K., Cui, L., Dong, Y., Wang, T., Da, C., Hirasaki, G. J., & Biswal, S. L. (2013). Adsorption of cationic and anionic surfactants on natural and synthetic carbonate materials. *Journal of Colloid and Interface Science*, 408, 164-172. <https://doi.org/10.1016/j.jcis.2013.07.006>
- [22] Massarweh, O., & Abushaikha, A. S. (2020). The use of surfactants in enhanced oil recovery: A review of recent advances. *Energy Reports*, 6, 3150-3178. <https://doi.org/10.1016/j.egy.2020.11.009>
- [23] McAuliffe, C. D. (1973). Crude-oil-Water emulsions to improve fluid flow in an oil reservoir. *Journal of Petroleum Technology*, 25(06), 721-726. <https://doi.org/10.2118/4370-pa>
- Pogaku, R., Mohd Fuat, N. H., Sakar, S., Cha, Z. W., Musa, N., Awang Tajudin, D. N., & Morris, L. O. (2017). Polymer flooding and its combinations with other chemical injection methods in enhanced oil recovery. *Polymer Bulletin*, 75(4), 1753-1774. <https://doi.org/10.1007/s00289-017-2106-z>
- [24] Pradhan, S., Kone, G., Antle, R., Aichele, C., Jiang, H., & Bikkina, P. (2018). Influence of Aspect Ratio and Wettability on Residual Oil Saturations after Waterflooding and Immiscible Gas Flooding: A Microfluidics Based Study. *International Symposium of the Society of Core Analysts*.
- [25] Royal Dutch Shell. (2013). Sustainability Report. <https://reports.shell.com/sustainability-report/2013/servicepages/welcome.html>
- [26] Saravanan, S., & Keerthana, S. (2017). Floquet instability of gravity-modulated salt fingering in a porous medium. *Industrial & Engineering Chemistry Research*, 56(10), 2851-2864. <https://doi.org/10.1021/acs.iecr.6b03866>
- [27] Schramm, L. L. (2014). *Emulsions, foams, suspensions, and aerosols: Microscience and applications*. John Wiley & Sons.

- [28] Sheng, James J. (2011): Modern chemical enhanced oil recovery. Theory and practice. Burlington, Mass.: Gulf Professional Publ.
- [29] Sun, C., Guo, H., Li, Y., & Song, K. (2020). Recent advances of surfactant-polymer (SP) flooding enhanced oil recovery Field tests in China. *Geofluids*, 2020, 1-16. <https://doi.org/10.1155/2020/8286706>
- [30] Suzuki, H. (1970). Determination of critical micelle concentration of surfactant by ultraviolet absorption spectra. *Journal of the American Oil Chemists Society*, 47(8), 273-277. <https://doi.org/10.1007/bf02609491>
- [31] Winsor, P. A. (1948). Hydrotrophy, solubilisation and related emulsification processes. *Transactions of the Faraday Society*, 44, 376. <https://doi.org/10.1039/tf9484400376>
- [32] Yang, W., Lu, J., Wei, B., Yu, H., & Liang, T. (2021). Model studies of surfactant flooding for enhanced oil recovery: A review. *ACS Omega*, 6(9), 6064-6069. <https://doi.org/10.1021/acsomega.0c05750>
- [33] Yousef, A. A., Al-Saleh, S., Al-Kaabi, A., & Al-Jawfi, M. (2011). Laboratory investigation of the impact of injection-water salinity and Ionic content on oil recovery from carbonate reservoirs. *SPE Reservoir Evaluation & Engineering*, 14(05), 578-593. <https://doi.org/10.2118/137634-pa>
- [34] Zhang, J., Gao, H., & Xue, Q. (2020). Potential applications of microbial enhanced oil recovery to heavy oil. *Critical Reviews in Biotechnology*, 40(4), 459-474. <https://doi.org/10.1080/07388551.2020.1739618>
- [35] Zhang, J., Yan, S., Yuan, D., Alici, G., Nguyen, N., Ebrahimi Warkiani, M., & Li, W. (2016). Fundamentals and applications of inertial microfluidics: A review. *Lab on a Chip*, 16(1), 10-34. <https://doi.org/10.1039/c5lc01159k>
- [36] Zhou, Y., Yin, D., Cao, R., & Zhang, C. (2018). The mechanism for pore-throat scale emulsion displacing residual oil after water flooding. *Journal of Petroleum Science and Engineering*, 163, 519-525. <https://doi.org/10.1016/j.petrol.2018.01.027>
- [37] Zulkifli, N. N., Mahmood, S. M., Akbari, S., Manap, A. A., Kechut, N. I., & Elrais, K. A. (2019). Evaluation of new surfactants for enhanced oil recovery applications in high-temperature reservoirs. *Journal of Petroleum Exploration and Production Technology*, 10(2), 283-296. <https://doi.org/10.1007/s13202-019-0713-y>

List of Figures

Figure 1. Projected global energy demand to 2050. (Royal Dutch Shell, 2013 [25]).....	15
Figure 2. Main methods of EOR (Massarweh & Abushaikha, 2020 [22])	19
Figure 3. Surfactant concentration below and above CMC, with respect to surfactant monomer concentration and IFT. (Lake, 2014 [18]).....	21
Figure 4. Winsor classification of microemulsions. (Winsor, 1948 [31]).....	22
Figure 5. Membrane Emulsification. (Akbari and Nour, 2018 [2])	26
Figure 6. Design of linear pore networks. (Pradhan et al., 2018 [24]).....	27
Figure 7. Effect of AR and Nca vs Sor. (Pradhan et al., 2018 [24])	28
Figure 8. Test-tube phase behavior experiments of a decane-surfactant solution system with increasing NaCl, top: experiment without contrast agents, bottom: simultaneous experiments (a) with and (b) without fluorescence contrast agent. (Kharrat et al., 2022 [16]).....	29
Figure 9. Smallscale test tubes with indicated NaCl concentration and positions at which SAXS measurements were taken. (Kharrat et al., 2022 [16])	30
Figure 10. One of oil mobilization mechanisms: Film thinning and drainage process. (Kharrat et al., 2022 [16]).....	30
Figure 11. Illustration of chip dimensions.	32
Figure 12. Empty pore systems, left: AR 3.2, $\lambda=100 \mu\text{m}$, right: AR 1.6, $\lambda=100 \mu\text{m}$	33
Figure 13. Empty pore system, AR 8 $\lambda=500 \mu\text{m}$	33
Figure 14. Area of entire oil filled pore (left), area of oil left in pore (right).	38
Figure 15. Distance measurement from position 0 till position x.	39
Figure 16. Oil filled pore system in binary using Image J.	40
Figure 17. Oil left at final stage in binary using Image J.....	40
Figure 18. Re for water and 2% NaCL surfactant injection for AR 1.6 and 3.2 vs pore diameters (radii).	42
Figure 19. Concave front and remaining oil for AR 1.6. Pictures are 1 second apart.	43
Figure 20. Concave front and remaining oil for AR 3.2. Pictures are 0.5 second apart.	43
Figure 21. Concave front and remaining oil for AR 4.5 Pictures are 0.5 seconds apart.	43
Figure 22. RF vs AR for DI injection	44
Figure 23. Final images in binary. Top: AR 1.6, middle: AR 3.2, bottom: AR 4.5. Almost complete bypass of 2 channels for AR 1.6 and 3.2. less bypass for AR 4.5	44
Figure 24. Initial front displacement: Alternating concave to convex with tiny emulsion droplets at the interfaces	46
Figure 25. Evolution of the shape of emulsions with time. Top left: tight orange bubbles in the oil phase and at surfactant-oil interface. Top right: loose solubilized foam-like flow. Bottom: final stage of experiment - emulsion with a high degree of solubility.....	46
Figure 26. Initial front displacement: Concave front. Time interval between pictures: 40 seconds. the two pictures are not taken at the same location.....	47
Figure 27. Formed emulsions in bottom channel , which experienced BT first. Top: Five seconds after BT, bottom: 30 seconds after BT.	47
Figure 28. Formed emulsions in top channel , which experienced BT later. Top: Five seconds after BT showing discrete bubbles, bottom: 30 seconds after BT, showing solubilized foam-like emulsion flow.....	48
Figure 29. Evolution of flow with time from slug flow to foam-like emulsion flow.	49
Figure 30. Initial front displacement: Concave front. Time between pictures: 1 second	49
Figure 31. Evolution of flow with. Time is increasing from top picture to bottom one. Complete solubilization achieved.....	50
Figure 32. Initial front displacement: Alternating concave to diagonal. Not trapped oil. No emulsions seen.	51
Figure 33. Emulsion formation with time.....	51
Figure 34. Initial front displacement: remained symmetrical concave with small bubble emulsions	52

Figure 35. Evolution of flow with time.....	52
Figure 36. Initial front displacement: remained symmetrical concave with small dot like emulsions trapped in the remaining oil.	53
Figure 37. Evolution of flow with time.....	53
Figure 38. AR 1.6, over-optimum case. Trapped oil reduces over time. Interval time: 15 minutes. Figure in binary from ImageJ.....	57
Figure 39. Average remaining oil saturation after first contact displacement with different ARs and injected fluid.....	57
Figure 40. DI injection RF with different ARs.	58
Figure 41. Evolution of in situ front velocities with time for different ARs and injected fluids.	59
Figure 42. Velocities wrt previous vs time and pore diameter (radius).	60
Figure 43. Velocity wrt previous vs. pore diameters (radii): 155, 96.7, and 125.85.	60
Figure 44. Velocities wrt previous vs time and pore diameter (radius).	61
Figure 45. Alteration of front shape from concave to convex (left to right).....	62
Figure 46. Velocities wrt previous vs time and pore diameter (radius).	62
Figure 47. Velocity wrt previous vs pore diameters (radii): 155, 96.7, and 125.85.	62
Figure 48. First contact displacement for $\lambda=500 \mu\text{m}$. Top: DI injection with concave front and no trapped oil. Middle: near-optimum condition with concave front. Bottom: over-optimum condition with concave front and emulsions in trapped oil and prior to the front	64
Figure 49. First contact displacement for $\lambda=2500 \mu\text{m}$. Top: DI injection with concave front and no trapped oil. Middle: near-optimum condition with concave front and no trapped oil. Bottom over-optimum condition with concave front and prior to the front.....	65
Figure 50. Different emulsion forms in different channels. Top: $\lambda=500$, over-optimum case Middle: $\lambda=500$, near-optimum case. Bottom: complete solubilization, $\lambda=500$ with near-optimum case	66
Figure 51. Initial displacement flow for high injection rate (0.005 ml/h) 1 (highest): AR=1.6, near-optimum case . 2: AR=1.6 over-optimum case. 3: AR=3.2 near-optimum case. 4 (lowest): AR=3.2, over-optimum case	68
Figure 52. Comparison of average remaining oil saturation for first contact displacement with different rates.	69
Figure 53. AR=3.2 with 2% surfactant injection. Different channels with different front velocities. The time interval between the pictures is 12.25 seconds.....	70
Figure 54. Slug flow preceding surfactant front.	70
Figure 55. Emulsions with high degree of solubility. Top: AR=1.6 with 2% surfactant injection. Bottom: AR=3.2 with 4% surfactant injection.....	71
Figure 56. First contact displacement for AR 1.6. Top row: DI injection with concave to diagonal front. Middle row: 3000 ppm Na_2CO_3 injection with alternating concave and convex front with dot-like emulsions. Bottom row: 7500 ppm Na_2CO_3 injection with concave front and "footprints".....	72
Figure 57. First contact displacement for AR 1.6. Top row: DI injection with concave front. Middle row: 3000 ppm Na_2CO_3 injection with concave front with dot like emulsions and "footprints". Bottom row: 7500 ppm Na_2CO_3 injection with concave front and "footprints".	73
Figure 58. AR 3.2 3000ppm injection, After BT still see footprints	74
Figure 59. Complex structure. Top: AR 3.2, 7500ppm Na_2CO_3 complex oil slug flow. Bottom: AR 1.6 7500 ppm Na_2CO_3 complex emulsions.	74
Figure 60. Trapped oil with AR 1.6 DI injection.....	75
Figure 61. Remaining oil saturation with different ARs and injected fluid. Top: average ROS during first contact displacement. Bottom: final RF.....	75

List of Tables

Table 1. Surfactant Classification is based on head charge.	20
Table 2. Winsor Classification.....	23
Table 3. Microfluidic chips design.	32
Table 4. Fluids used.....	34
Table 5. Oil 16 properties.	35
Table 6. Injected fluid properties.....	40
Table 7. Same distance between pores ($\lambda=100 \mu\text{m}$) and different AR 42	42
Table 8. First contact displacement characteristics for 2% NaCl surfactant injection and different ARs.....	45
Table 9. First contact displacement characteristics comparison for 4% NaCl surfactant solution injection in different ARs.....	50
Table 10. Emulsion comparison between different ARs and injected fluid.....	55
Table 11. Comparison between different ARs and injected fluid.	56
Table 12 Front velocities wrt initial in $\mu\text{m/s}$	58
Table 13. Description of all flow parameters for AR 1.6 with DI, 2%, and 4% injection.	63
Table 14. Comparison between different λ s and injected fluid.....	64
Table 15. Comparison between different injection rates, ARs, and injected fluid.	67
Table 16. Comparison between different ARs and injected fluid for oil 16.	71
Table 17. Summary of all experiments in terms of flow characteristics.....	76

Nomenclature

v	Velocity	[$\mu\text{m}/\text{sec}$]
d	Distance	[μm]
t	Time	[sec]
Re	Reynold's number	
ρ	Density	[kg/m ³]
d	Diameter	[m]
μ	Viscosity	[Pa.s]
λ	Distance between pores	[μm]
P_b	Pore body	[μm]
P_t	Pore throat	[μm]

Abbreviations

Avg ROS	Average remaining oil saturation
AR	Aspect ratio
BT	Breakthrough
IFT	Interfacial tension